Corrosion Science 265 (2026) 113819

Contents lists available at ScienceDirect

Corrosion Science

journal homepage: www.elsevier.com/locate/corsci

Enhancing corrosion resistance of Mg-Zn-Ca alloys via constrained friction processing

Ting Chen [a,*], Banglong Fu [a,b,**], Bahram Vaghefinazari [c], Uceu F.H.R. Suhuddin [a], Yulong Wu [c], Tong Shen [a], Emad Maawad [d], Sviatlana V. Lamaka [c], Jorge F. dos Santos [a,e], Mikhail L. Zheludkevich [c,f], Jean Pierre Bergmann [g], Benjamin Klusemann [a,h]

[a] Solid State Materials Processing, Institute of Material and Process Design, Helmholtz-Zentrum Hereon, Max-Planck-Str. 1, Geesthacht 21502, Germany
[b] School of Materials Science and Engineering, Shandong University, Jingshi Road 17923, Jinan 250061, China
[c] Institute of Surface Science, Helmholtz-Zentrum Hereon, Max-Planck Str. 1, Geesthacht 21502, Germany
[d] Institute of Materials Physics, Helmholtz-Zentrum Hereon, Max-Planck-Str. 1, Geesthacht 21502, Germany
[e] FSW Engineering and Technology Center, STIRTEC GmbH, Kalsdorf bei Graz 8141, Austria
[f] Institute of Materials Science, Kiel University, Kaiserstraße 2, Kiel 24143, Germany
[g] Production Technology Group, Technische Universität Ilmenau, Gustav-Kirchhoff-Platz 2, Ilmenau 98693, Germany
[h] Institute for Production Technology and Systems, Leuphana University Lüneburg, Universitätsallee 1, Lüneburg 21335, Germany

ARTICLE INFO

Keywords:
Mg alloys
Constrained friction processing
Corrosion resistance
Microstructure

ABSTRACT

Magnesium (Mg) alloys are promising lightweight structural materials due to their excellent mechanical properties and high specific strength. However, their relatively high corrosion rates, susceptibility to localized corrosion, and potential for stress corrosion cracking pose significant challenges for engineering applications. This study investigates the corrosion resistance of Mg-Zn-Ca (ZX) alloys processed by a constrained friction processing (CFP) technique. CFP significantly refines the microstructure, reduces the size and volume of secondary phases, and enhances the mechanical properties of ZX alloys. The results show that CFP ZX alloys exhibit improved corrosion resistance in NaCl solution, with ZX10 alloy demonstrating the best performance due to the formation of a dense corrosion product and a protective Zn-rich layer on the surface. The study reveals that the severe shear deformation and extensive recrystallization during CFP accelerate the dissolution of secondary phases into the matrix, leading to a more homogeneous microstructure and reduced localized micro-galvanic corrosion. These findings highlight the potential of CFP for producing high-performance Mg alloys with enhanced corrosion resistance for structural applications.

1. Introduction

Magnesium (Mg) alloys have attracted extensive attention as lightweight structural materials due to their exceptionally low density, high specific strength, and favorable damping and machinability characteristics [1]. Their very low density (1.74 ~ 2.00 g/cm^3) and high specific strength enables significant mass reduction in applications where weight efficiency is crucial, such as transportation, aerospace, electronics, and other emerging lightweight engineering systems [2]. In addition, the intrinsic biodegradability and good biocompatibility of Mg alloys have also enabled their exploration in biodegradable implant devices as an extended application scenario [3,4].

Despite these advantages, Mg alloys exhibit relatively high corrosion rates in aqueous or humid environments due to their low electrode potential (−1.7 ~ −1.3 V vs. SHE), which limits their long-term performance and structural reliability [5]. Localized corrosion and stress-corrosion cracking may further compromise mechanical integrity, posing challenges for their use in demanding service environments [6]. Therefore, improving corrosion resistance while maintaining desirable mechanical properties, particularly high specific strength, remains a central objective in the development and broader application of advanced Mg alloys.

Microstructural characteristics, including grain size and the morphology and distribution of secondary phases, significantly affect

* Corresponding author.
** Corresponding author at: School of Materials Science and Engineering, Shandong University, Jingshi Road 17923, Jinan 250061, China.
E-mail addresses: ting.chen@hereon.de (T. Chen), bl.fu@email.sdu.edu.cn (B. Fu).

https://doi.org/10.1016/j.corsci.2026.113819
Received 9 December 2025; Received in revised form 20 March 2026; Accepted 27 March 2026
Available online 27 March 2026

both mechanical behavior and corrosion performance. Alloying is one of the most effective strategies to tailor these microstructures [7]. Calcium (Ca) and zinc (Zn) are popular alloying elements in Mg alloys, since Ca and Zn can help to improve both corrosion resistance and mechanical properties. Zn has been reported to enhance mechanical properties and corrosion resistance through solid solution strengthening and stabilizing the corrosion film [8]. However, excessive Zn (>4 wt%) reduces tensile strength and elongation, as well as corrosion resistance [9]. Ca is known to refine microstructure and improve strength but can form brittle intermetallic phases that accelerate corrosion [10]. Combining Zn and Ca in low concentrations (≤1 wt%) has shown promise in balancing mechanical and corrosion properties [11,12].

In addition to alloying, microstructure refinement through severe plastic deformation (SPD) techniques, such as equal-channel angular pressing (ECAP) and high-pressure torsion (HPT), has improved mechanical properties and corrosion resistance. For example, Ma et al. [13] achieved ultra-fine grains in ZE41A alloys via ECAP, enhancing strength and ductility. Yang et al. [14] observed improved corrosion resistance in AZ91 after ECAP due to reduced β-phase particles and weakened galvanic effects. HPT has also been used to produce ultra-fine-grained Mg alloys with enhanced mechanical properties and corrosion resistance [15,16]. However, SPD methods often result in inhomogeneous microstructures, requiring multiple passes or homogenization heat treatment, which reduce production efficiency and increase energy consumption [17–19].

Friction-based techniques, such as friction stir processing (FSP), offer efficient microstructural refinement and homogenization. Zhang et al. [20] reported refined grains and improved corrosion resistance in Mg-Nd-Zn after FSP. Shunmugasamy et al. [21] found that FSPed EZ33 alloy exhibited enhanced hardness, ductility, and stable corrosion rates, with favorable osseointegration and no toxic byproducts. To further advance high-performance Mg alloys, constrained friction processing (CFP) has been developed [22]. CFP eliminates the need for pre-processing steps, generates heat internally, achieves refined microstructures and improves mechanical properties significantly in a short production cycle (≤ 3 s) [23,24]. This method offers high efficiency, cost savings, and energy conservation, making it a promising approach for producing high-performance Mg alloys for structural and lightweight engineering applications.

In the present study, corrosion resistance of ZX alloys after CFP was investigated. The type and size of the secondary phase in ZX alloys before and after CFP were characterized, and the evolution of the secondary phase during CFP was analyzed since the secondary phase is closely related to corrosion resistance and mechanism. Then, the corrosion rate was measured, and the corrosion product after the corrosion test was characterized to understand the corrosion mechanism.

2. Materials and Method

The base material (BM) in this study consisted of chill-cast Mg-Zn-Ca (ZX) alloy ingots with varying Zn contents, produced at Helmholtz Zentrum Hereon (Germany). The chemical compositions of the as-cast (AC) ZX alloys, including ZX00, ZX10, and ZX20, measured using SPECTROALB M12 spark atomic emission spectroscopy, are detailed in Table 1. The average grain size in the as-cast ZX alloys exceeds 1 mm. The ingots were cut into plates with dimensions 100 × 25 × 6 mm^3 for subsequent CFP processing.

CFP was conducted using the RPS 200 system from Harms & Wende (Hamburg, Germany). The tool and procedure for CFP have been described in our previous work [25], for more details see Fig. S1. The tool system comprises a clamping ring (CR), a shoulder, and a probe, with diameters of 17 mm, 9 mm, and 6 mm, respectively, as shown in Fig. S1(a). The detailed processing procedures are shown in Fig. S1(b) and (c), with the corresponding parameters listed in Table 2. The procedure of single pass CFP (SP-CFP) can be divided into three stages, Fig. S1(b): 1) Preparation stage: The clamping ring descends and applies a pre-set force to secure the BM against the backing anvil; 2) Plunging stage: The shoulder and probe begin rotating at a predetermined speed. Simultaneously, the shoulder plunges into the BM while the probe ascends, ensuring material volume remains balanced; 3) Final stage, when the shoulder arrives at the pre-set plunge depth, the tool system stops rotating and retracts. This results in a processed rod with a diameter equal to that of the probe. Compared to SP-CFP, double pass CFP (DP-CFP) introduces one additional processing cycle that includes plunging and retraction stages. During the retraction stage, the shoulder and probe rotate as they return to their initial positions. Based on our prior study, DP-CFP demonstrated a more pronounced improvement in mechanical properties, and thus ZX alloys with different Zn contents were processed using the DP-CFP, which involves an initial pass with high heat input followed by a second pass with low heat input. In addition, SP-CFP with two levels of heat input, as well as DP-CFP, were applied to the ZX10 alloy to further investigate the effects of processing parameters. The corresponding parameters, including rotation speed (RS), plunge depth (PD) and plunge time (PT), are listed in Table 2.

During the CFP process, the thermal profile was monitored using K-type thermocouples enclosed in a 0.5 mm diameter metal sheath. The thermocouples were positioned along the probe centerline, 3.5 mm beneath the top surface of the base metal sheet and roughly 0.5 mm away from the depth to which the tool was plunged.

After the CFP procedure, the longitudinal section of the processed rod was cut and subsequently ground and polished in accordance with conventional metallographic preparation routines. The microstructure was examined using an FEI Quanta 650 field-emission SEM equipped with an EDAX Apollo X EDS system and Velocity detectors for EBSD acquisition. Prior to EBSD measurements, the specimens were electropolished in AC2 solution (Struers A/S, Ballerup, Denmark) at −20 °C under an applied voltage of 25 V for approximately 35 s. The resulting EBSD datasets were then processed and evaluated using TSL OIM 8 and MTEX 5.10 software packages. The phases within the as-cast and CFP ZX alloys were identified by high-energy synchrotron X-ray diffraction (HE-XRD) technique, conducted at P07 beamline of PETRA III, Deutsches

Table 2
Processing parameter of CFP for SP- and DP CFP at different heat inputs.

Processing Parameters	1st Pass			2nd Pass		
	RS /rpm	PD /mm	PT /s	RS /rpm	PD /mm	PT /s
SP-CFP (low heat)	1800	3	1	-	-	-
SP-CFP (high heat)	2400	3	1	-	-	-
DP-CFP	2400	3	1	1800	3	1

Table 1
Chemical compositions of as-cast ZX alloys, as provided by spark atomic emission spectrometry.

Materials	Chemical Composition /wt%							
	Mg	Zn	Ca	Fe	Cu	Ni	Al	Si
ZX00	Bal.	0.49	0.32	0.0010	0.0002	0.0005	0.0024	0.0034
ZX10	Bal.	0.97	0.30	0.0012	0.0002	0.0005	0.0055	0.0061
ZX20	Bal.	1.93	0.31	0.0011	0.0003	0.0005	0.0020	0.0051

Elektronen-Synchrotron (DESY, Hamburg, Germany). The experimental system is shown in Fig. S2. Different ZX alloy samples were examined in transmission mode by a monochromatic X-ray beam with an energy of 103.8 keV and a size of 0.5 × 0.5 mm^2. The collected 2D diffraction patterns were further integrated by Fit2D [26] to obtain the 1D diffractograms. Finally, the diffraction patterns were analyzed and assigned by referencing the Powder Diffraction File (PDF) entries for the relevant phases obtained from the International Centre for Diffraction Data (ICDD) database.

To preliminarily investigate the effects of different Zn contents and the CFP process on corrosion resistance, the corrosion rates of the samples in stirred NaCl solution were measured using hydrogen evolution experiments as well as mass loss experiments. Hydrogen evolution experiments were performed using eudiometers (art. nr. 2591–10–500, Neubert-Glas, Germany). The experimental setup has been described in detail in [27]. The surfaces of all samples were ground to 1200 grit before the hydrogen evolution experiments. Three samples, with a total surface area of 500 mm^2, were placed in each eudiometer bottle containing 500 mL of 0.9% (w/v) NaCl solution (normal saline) for 72 h. Throughout the tests, the corrosive medium was continuously agitated using a magnetic stirrer. Each condition was tested in triplicate to ensure reliability. The collected hydrogen volume was converted to the corresponding amount of dissolved alloy, 1 mL of hydrogen released = 0.001004 g of alloy loss done, the contribution of oxygen reduction to the cathodic reaction is negligible. The average corrosion rate derived from H_2 evolution, CR_H /mm·yr^{-1}, of each condition was calculated using:

$$CR_H = \frac{0.001004 \quad g/mL \bullet \Delta V}{\rho \bullet A \bullet t} \tag{1}$$

where ΔV /mL is the volume of H_2 produced during immersion, ρ /g·cm^{-3} is the density of the Mg alloys, A /cm^2 is the exposed surface area, and t /yr is the immersion duration. After immersion, corrosion products were removed in a chromic acid solution (180 g/L chromium (VI) oxide in distilled water, VWR International, Darmstadt, Germany) for 20 min at room temperature to determine the weight loss, ΔW /g, and the average corrosion rate measured by weight loss, CR_W, was calculated using:

$$CR_W = \frac{\Delta W}{\rho \bullet A \bullet t} \tag{2}$$

After the immersion test, the corroded surface and the cross-sectional morphologies were characterized by FEI Quanta 650 field emission gun (FEG) SEM equipped with EDAX Apollo X energy dispersive spectroscopy (EDS). The microstructural analysis was further carried out using FEI Talos F200X G2 transmission electron microscope (TEM) to investigate the corrosion product. Additionally, after the removal of corrosion products by immersion in chromic acid, the variation of corroded surface height was measured using Keyence 3D laser scanning microscope VR-5200, and the pitting factor was calculated according to ASTM G46–94. Moreover, the surface morphology was further characterized by the FEI Quanta 650 field emission gun (FEG) SEM equipped with EDAX Apollo X energy dispersive spectroscopy (EDS).

The corrosion behaviors of the studied alloys were analyzed using electrochemical measurements with a Gamry potentiostat/frequency response analyzer system. A typical three-electrode cell was employed, consisting of a coiled platinum wire electrode, an Ag/AgCl reference electrode in saturated KCl, and the specimen as the working electrode. The cross-sectional surface of the sample was chosen as the exposed area, with a size of 0.25 cm^2. All measurements were conducted under atmospheric conditions using 400 mL 0.9 wt% NaCl solution as the corrosive electrolyte. The samples for the electrochemical studies were ground to 1200 grit. Each condition was tested at least three times to ensure the reproducibility of the results. Open circuit potential (OCP) is the potential of a working electrode relative to the reference electrode when no external potential or current is applied to the cell. In this study, the open-circuit potential (OCP) of the samples was monitored for 30 min before performing potentiodynamic polarization (PDP) measurements to ensure the potential reached a stable condition. Potentiodynamic polarization tests were then carried out to investigate differences in the instantaneous polarization behavior of the alloys. The cathodic scans started at + 50 mV relative to the OCP and proceeded to −1000 mV, with a scan rate of 1 mV/s. Electrochemical impedance spectroscopy (EIS) was employed to examine the corrosion mechanisms and the properties of the interfacial layer formed on the metal surface in the electrolyte. EIS measurements were conducted at OCP using a 10 mV rms sinusoidal perturbation over a frequency range from 100 kHz down to 0.01 Hz. Prior to impedance testing, the samples were maintained at OCP for 30 min to stabilize the potential. The acquired impedance data were fitted and analyzed using ZView software, with Chi-squared values below 0.001 to ensure data reliability.

3. Results

3.1. Microstructure

Fig. S3 illustrates the macrostructural overview of a ZX10 alloy specimen processed via CFP. The rod, characterized by fine grains, is subjected to intense stirring during CFP, leading to the development of a distinct stir zone (SZ). Immediately adjacent to the SZ, a partially deformed region, known as the thermo-mechanically affected zone (TMAZ), exists between the SZ and the BM. This zone reflects a gradual attenuation of the combined mechanical and thermal influences from the rod toward the BM.

The corrosion resistance of ZX alloys is closely related to their microstructure, especially the grain size, as well as the type and size of the secondary phases. The microstructure of the as-cast ZX alloys and the SZ in CFPed ZX alloys was characterized by SEM and EBSD, as shown in Fig. 1. The chemical composition of the estimated secondary phases in Fig. 1 is listed in Table 3. HE-XRD by synchrotron radiation was also carried out to investigate the type of secondary phase in ZX alloys, as shown in Fig. 2. Additionally, the equilibrium thermodynamic of ZX00, ZX10 and ZX20 alloys was calculated by JMatPro 4.1.7, as shown in Fig. S4, to verify the possible phase in as-cast and CFPed ZX alloys. In as-cast ZX00 alloy, a small number of coarse Mg_2Ca and $Mg_6Zn_3Ca_2$ particles were observed, see Fig. 1(a) and (b), presenting small corresponding peaks in the integrated diffraction profiles, see Fig. 2(b). After DP-CFP, the average grain size (GS) decreased significantly to about 5 μm. No secondary phase was observed by SEM in DP-CFPed ZX00 alloy, and the integrated diffraction profiles in Fig. 2(a) did not exhibit extra peaks except for Mg peaks, indicating the complete dissolution of secondary phase during processing. Similarly, as-cast ZX10 alloy exhibited Mg_2Ca and $Mg_6Zn_3Ca_2$ particles, which are larger in size and show a higher volume than in as-cast ZX00 alloy. When SP-CFP with lower heat input, i.e. rotation speed of 1800 rpm, was adopted, the secondary phase in ZX10 alloy transformed to fine Mg_2Ca particles. There was no observable secondary phase in ZX10 after SP-CFP with higher heat input, i.e. rotation speed of 2400 rpm, and DP-CFP. The GS of ZX10 after SP-CFP with low heat input and DP-CFP were similar (about 5 μm), but GS of ZX10 after SP-CFP with high heat input was significantly higher (about 10 μm). As-cast ZX20 alloy exhibited larger eutectic secondary phases, including $Mg_6Zn_3Ca_2$ and $Mg_5Zn_{13}Ca_2$. Different from the other ZX alloys processed by DP-CFP, the DP-CFPed ZX20 alloy exhibited higher Ca and Zn concentrations along the refined grain boundaries. Fig. 3 shows the TEM results of ZX00 and ZX10 alloys after DP-CFP. It has been reported that most secondary phases in Mg-Zn-Ca alloys exhibit a plate- or disk-like morphology, aligning parallel to the (0002) plane of α-Mg [28]. Therefore, in TEM observations, the z-axis is kept parallel to (0002) of α-Mg to ensure the visibility of these precipitates. No secondary phase was observed in DP-CFPed ZX00 and ZX10 alloys, verifying the complete dissolution of secondary phase

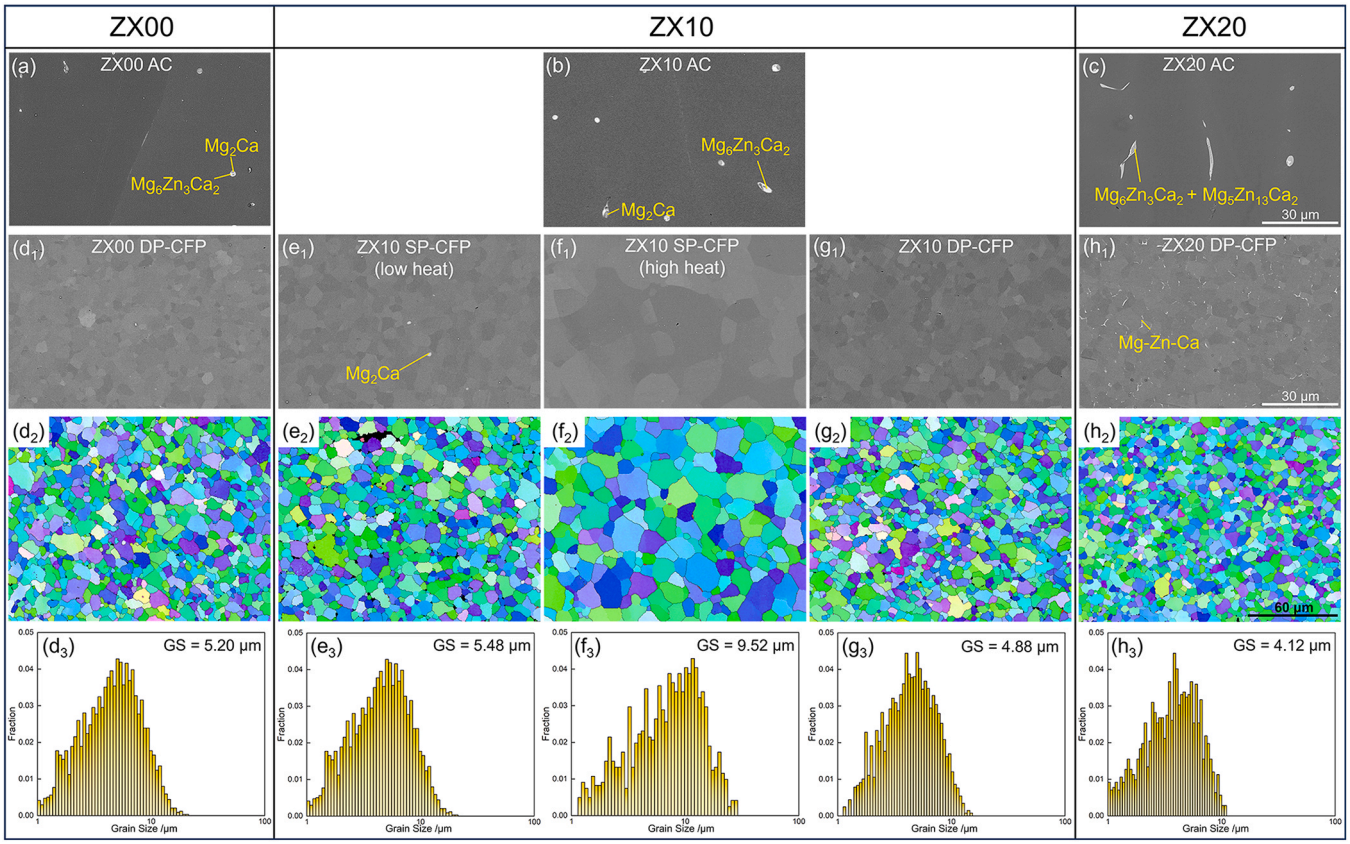

Fig. 1. Microstructure of as-cast (a) ZX00, (b) ZX10, (c) ZX20, and (d_1) ZX00 after DP-CFP, (e_1) ZX10 after SP-CFP with low heat input, (f_1) ZX10 after SP-CFP with high heat input, (g_1) ZX10 after DP-CFP, (h_1) ZX20 after DP-CFP. (d_2)-(h_2) Corresponding EBSD maps with (d_3)-(h_3) grain size distribution.

Table 3
Chemical composition of the estimated secondary phases in Fig. 1.

Sample	Secondary phase	Chemical composition by EDS analysis /at%		
		Mg	Zn	Ca
ZX00 AC	$Mg_6Zn_3Ca_2$	75.6	13.2	11.2
	Mg_2Ca	75.9	3.5	20.6
ZX10 AC	$Mg_6Zn_3Ca_2$	61.4	24.6	13.9
	Mg_2Ca	82.9	1.3	15.8
ZX10 SP-CFP (1800 rpm)	Mg_2Ca	71.6	2.6	25.8
ZX20 AC	$Mg_6Zn_3Ca_2 + Mg_5Zn_{13}Ca_2$	63.2	24.3	12.5
ZX20 DP-CFP	Mg-Zn-Ca	94.0	3.0	3.0

Note: No secondary phase was observed in DP-CFPed ZX00, SP-CFPed ZX10 with high heat input and DP-CFPed ZX10.

in ZX00 and ZX10 alloys during the DP-CFP. The adoption of CFP could not only decrease the grain size of ZX alloys but also decrease the size and the volume of the secondary phase within a very short processing time.

3.2. Corrosion rate

Hydrogen evolution as well as weight loss tests were conducted in continuously stirred 0.9% NaCl solution to measure the corrosion rate of different ZX alloys before and after CFP, serving as a preliminary evaluation of the effects of CFP and Zn content on their corrosion behavior, as shown in Fig. 4. Comparing the as-cast ZX alloys with different Zn contents, as-cast ZX00 alloy exhibited the best corrosion resistance from the investigated alloys. As the Zn content of ZX alloys increased, the corrosion rate of ZX alloys increased significantly, from about 1.7 mm/yr in ZX00 alloy to about 3.2 mm/yr in ZX10 alloy and 3.5 mm/yr in ZX20 alloy. After CFP was carried out on these ZX alloys, the corrosion rate of ZX alloys, especially ZX00 alloy and ZX10 alloy, decreased significantly. The corrosion rate of ZX00 alloy after DP-CFP decreased to about 0.8 mm/yr, by 53%. ZX10 alloy after DP-CFP exhibited the best corrosion resistance in this study, the corrosion rate decreased to about 0.5 mm/yr, a reduction by 84% compared with the as-cast state. Although the measured corrosion rates after processing are relatively high due to the accelerated corrosion caused by corrosive media stirring, the overall significant decrease clearly demonstrates the important role of CFP in improving corrosion resistance. A systematic discrepancy between CR_W and CR_H might be ascribed to solubility of H_2 in the 0.9% NaCl aqueous solution and contribution of oxygen reduction reaction to the total cathodic process [29]. In order to demonstrate the corrosion behavior of the CFPed ZX alloys, the DP-CFPed ZX10 alloy, with lowest corrosion rate among the investigated alloys, was tested in static 3.5 wt % NaCl media, a standard environment frequently used for corrosion rate measurements in Section 4.3.

The corrosion resistance of ZX10 alloy after SP-CFP with different heat inputs and DP-CFP was similar, indicating that the grain size and existence of fine Mg_2Ca particles did not affect the corrosion resistance significantly. The improvement of corrosion resistance might be attributed to the significant decrease of secondary phase particles by CFP, see Fig. 1, and galvanic corrosion [30]. In the case of ZX20 alloy, the corrosion rate slightly decreased after DP-CFP. Compared with DP-CFPed ZX00 and ZX10, the corrosion rate of DP-CFPed ZX20 was much higher, which might be attributed to the micro-galvanic corrosion [31] associated with higher Ca and Zn elements concentration along the refined grain boundaries, as shown in Fig. 1(h_1). The localized enrichment of these elements at the grain boundaries leads to a significant potential difference between the grain boundary and the grain interior, thereby promoting micro-galvanic coupling and accelerating corrosion [32].

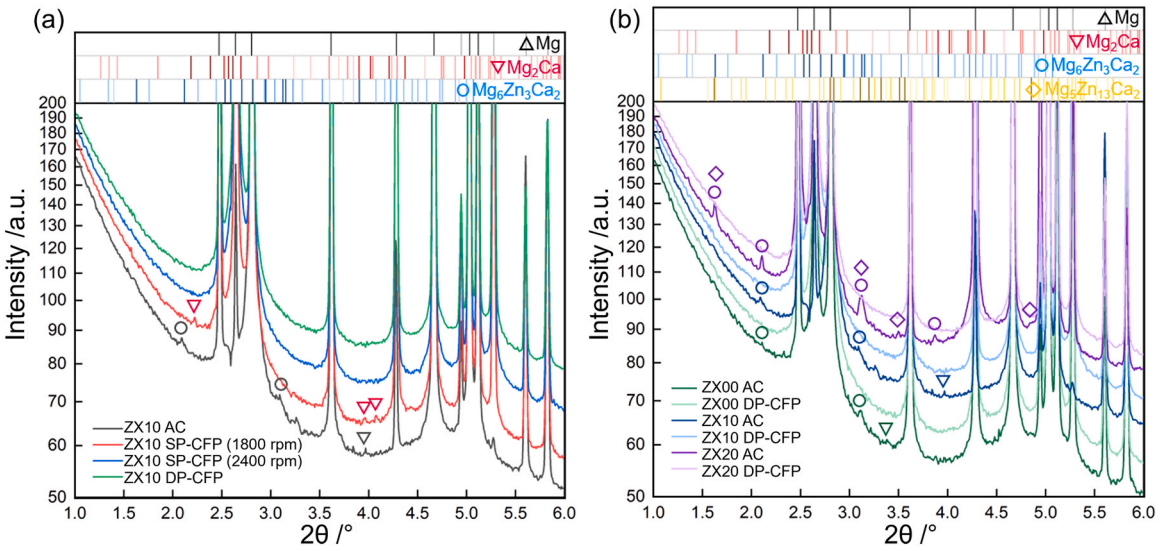

Fig. 2. Integrated diffraction profiles obtained from synchrotron radiation for: (a) as-cast ZX10 and ZX10 samples processed by CFP under different processing parameters, and (b) different as- cast ZX alloys and ZX alloys after DP-CFP. The corresponding positions of Bragg peaks, which are calculated according to the referred PDF numbers of ICDD, are also indicated.

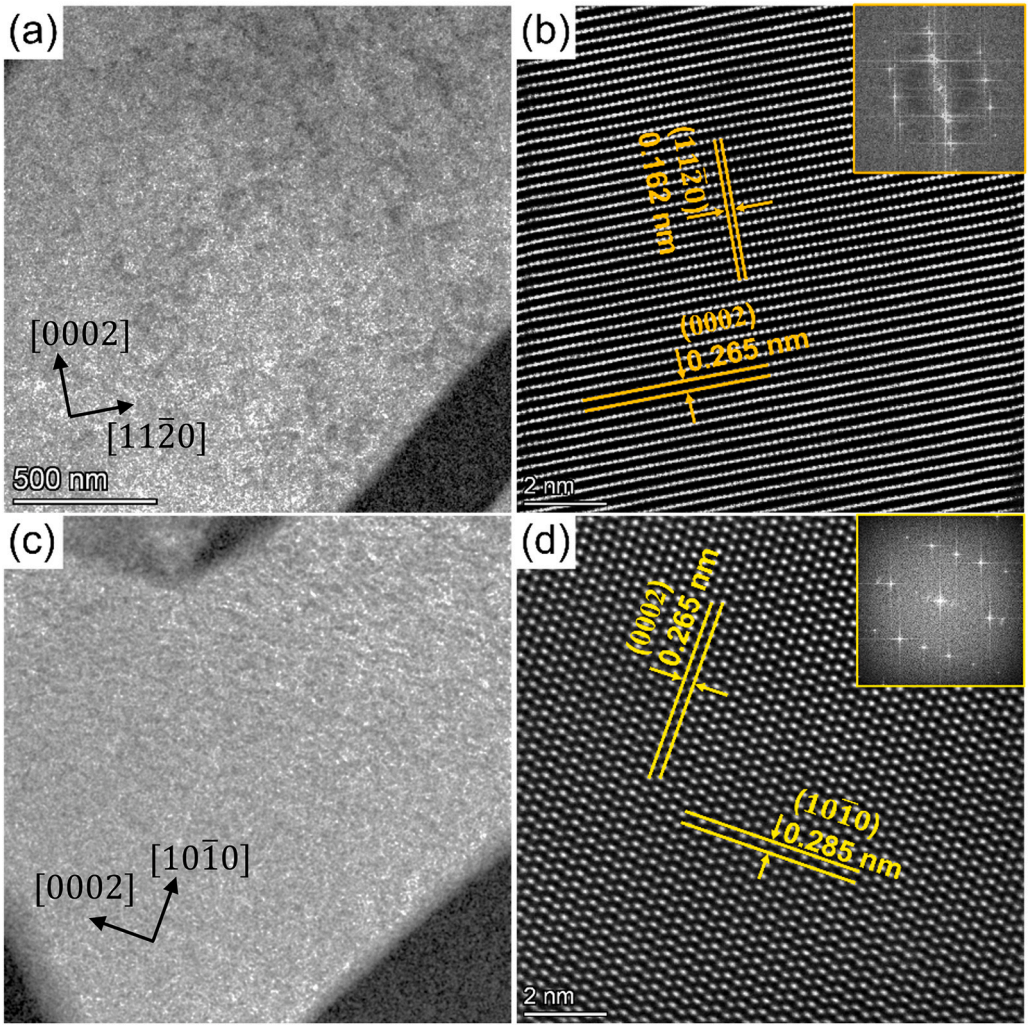

Fig. 3. TEM results of (a)(b) DP-CFPed ZX00 and (c)(d) DP-CFPed ZX10.

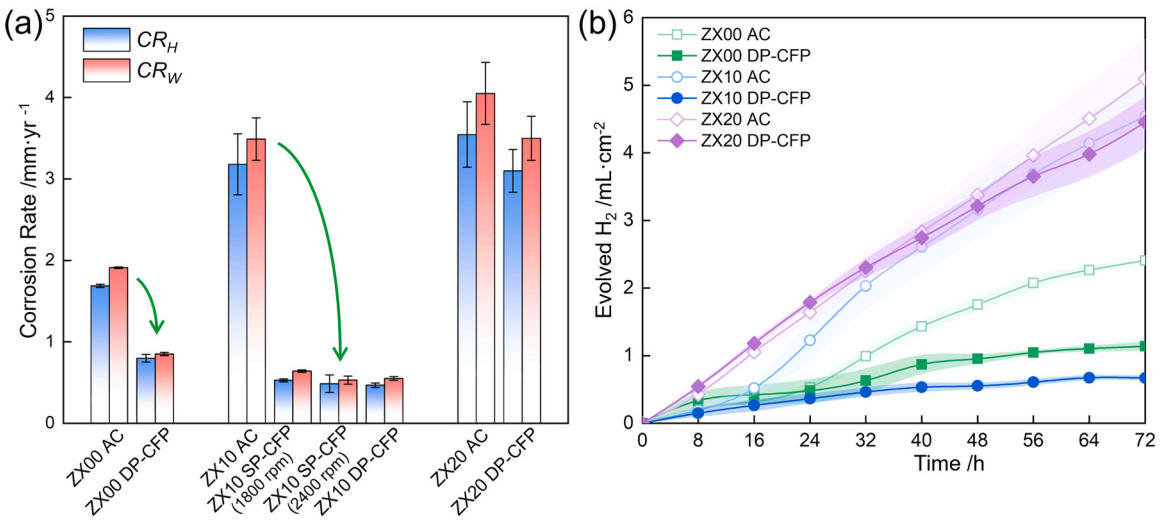

Fig. 4. Corrosion rate of different ZX alloys by hydrogen evolution (CR_H) and weight loss (CR_W) tests in 0.9% NaCl solution. (a) Corrosion rate for 3 days and (b) H_2 evolution during the test. The shaded regions represent the standard deviation of measurements.

3.3. Electrochemical measurements

To further investigate the effect of the CFP process on the corrosion resistance mechanism, electrochemical tests were carried out on different ZX alloys processed by the DP-CFP route, which had shown the best improvement in mechanical properties.

To understand the corrosion kinetics, Fig. 5(a) show the OCP results of as-cast ZX alloys and DP-CFPed ZX alloys during immersion in 0.9% NaCl for 30 min. All curves present similar characteristics. The OCP values dropped slightly at the initial stage, then gradually increased with extended immersion time throughout the entire testing period. The potential of as-cast ZX alloys increased as the Zn content increased. After DP-CFP, the potential of ZX00 and ZX10 alloys decreased significantly, which might be attributed to solid solution of the secondary phase particles, including Ca, during processing. However, the potential of DP-CFPed ZX20 alloy remained similar to that of as-cast ZX20 alloy. In order to understand the corrosion kinetics for ZX alloys before and after DP-CFP, PDP measurements were carried out on as-cast and DP-CFPed ZX alloys, and the cathodic polarization curves are shown in Fig. 5(b). As shown in Fig. 5(b), all ZX alloys with different Zn contents and before or after DP-CFP exhibit similar cathodic behavior in the initial stage of corrosion, indicating that the hydrogen evolution kinetics show no significant differences among these materials at this early stage.

In order to investigate the barrier property of the corrosion product films on the surface of corroded ZX alloys, EIS measurements were carried out on ZX alloys immersed in 0.9% NaCl solution for 6 h and 24 h. After 6 h immersion, the Bode plots clearly present two time-constants, which correspond to the two capacitive loops in Fig. 6(b_1). The first one at high-frequency (HF) can be related to the MgO-based surface film resistance in parallel with the MgO film capacitance, and the second one appeared at middle-frequency (MF) is attributed to the charge transfer resistance [33]. At the low frequencies, a pseudo-inductive response was observed, which is typically related to the non-stationarities often observed during the corrosion of Mg-based systems [34]. As shown in Fig. 6(a_1), the impedance modulus values of all tested Mg alloys at middle to low frequencies, especially that of ZX00 and ZX10 alloys, were increased following CFP processing. This suggests that the CFP technique offers a generally applicable strategy for improving the corrosion resistance of Mg alloys [35,36]. To investigate the contribution of the corrosion product film formed at the interface to the improvement in corrosion resistance, the EIS results were fitted using the equivalent circuit model shown in Fig. 6(b_1). R_{sol} is the solution resistance, R_{ox} is the resistance of the oxide film, and R_{ct} is the charge transfer resistance. The CPE_{ox} with n_{ox}, and CPE_{dl} with n_{dl} describe constant phase elements matched with R_{ox} and R_{ct}, respectively. The detailed fitting parameters and their estimated errors are

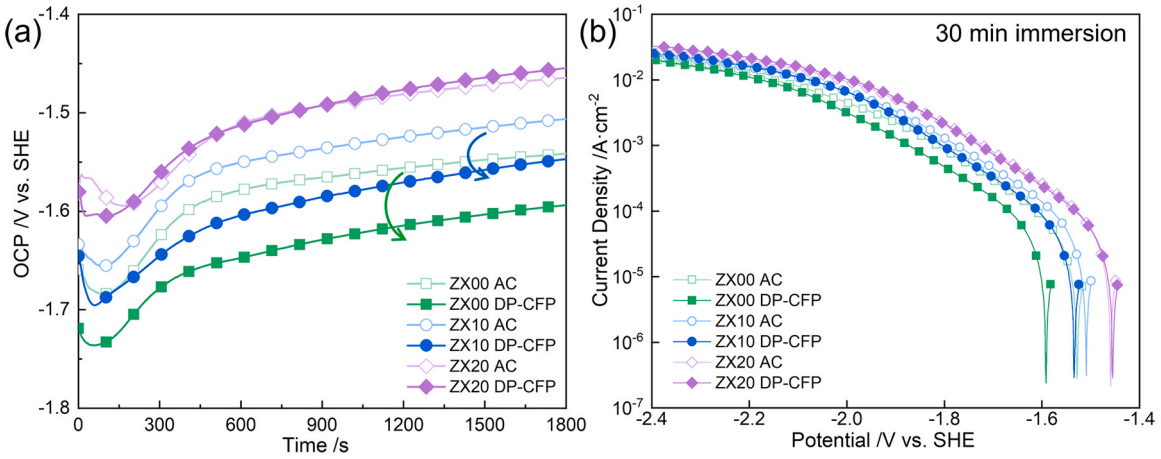

Fig. 5. (a) Open circuit potential (OCP) curves of as-cast ZX alloys and DP-CFPed ZX alloys during immersion in 0.9% NaCl for 30 min. (b) cathodic polarization curves of as-cast ZX alloys and DP-CFPed ZX alloys after immersion in 0.9% NaCl for 30 min.

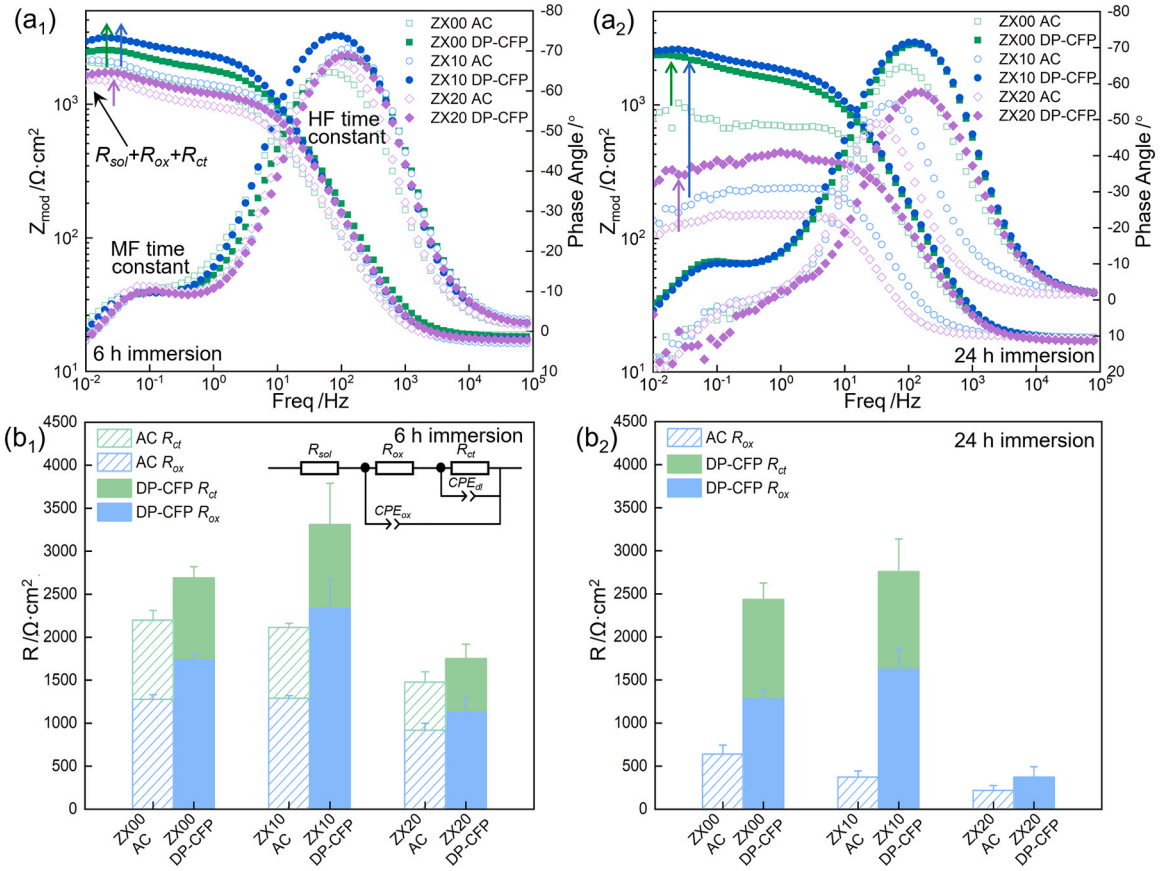

Fig. 6. EIS spectra of as-cast ZX alloys and DP-CFPed ZX alloys immersed in 0.9% NaCl for (a_1-b_1) 6 h and (a_2-b_2) 24 h. (a) Bode plot, (b) resistances charge transfer and surface film obtained by adopting the equivalent circuit illustrated in (b_1).

provided in Table 4 and Table S1. An example of the experimental Bode spectrum and the corresponding fitting curve is presented in Fig. S1. After CFP treatment, the enhanced corrosion resistance of the Mg alloys is primarily attributed to the formation of oxide layers with higher resistance [37,38], as shown in Fig. 6(b_1). After immersion for 24 h, the impedance modulus values of all tested Mg alloys, especially ZX00 and ZX10 alloys, was still enhanced following CFP processing, as shown in Fig. 6(a_2). The EIS spectra of the CFPed ZX00 and ZX10 alloys still exhibited two time-constants after 24 h, whereas those of all as-cast ZX alloys and the CFPed ZX20 alloy exhibited unstable low-frequency response with scattering and inductive characteristics due to apparent non-stationarities [34]. In such cases, only the high-frequency capacitive loop was fitted to evaluate R_{ox}. Compared with 6 h immersion results, the R_{ox} values of all tested as-cast ZX alloys and CFPed ZX20 alloy decreased significantly after 24 h, indicating that the protective performance of the oxide film deteriorated quickly with continued corrosion in the chloride electrolyte. In contrast, the R_{ox} of the CFPed ZX00 and ZX10 alloys remained much higher than that of their as-cast counterparts, as shown in Fig. 6(b_2), suggesting that their protective oxide films were more stable over time, thereby conferring superior long-term corrosion resistance.

3.4. Corrosion morphology and product analysis

Corrosion morphology and corrosion products are closely related to corrosion resistance. After corrosion under stirring 0.9% NaCl solution for 3 days, the morphology of the corrosion product layer on the surface of different ZX alloys was characterized by SEM, as shown in Fig. 7. In order to investigate the morphology of the underlying substrate after corrosion, ZX alloys were cleaned with chromic acid to remove the corrosion layers and characterized by an optical profilometer, SEM with EDS, as shown in Fig. 8 and Fig. 9. The surface of as-cast ZX alloys with different Zn contents after corrosion for 3 days exhibited deep localized corrosion and shaped shallow grooves around them with high pitting factor (more than 20), as shown in Fig. 8 and Fig. 9(a-c), which may be related to the micro-galvanic interactions that could serve as

Table 4
Fitted parameters based on electrochemical impedance spectra of as-cast ZX alloys and DP-CFPed ZX alloys after 6 h immersion.

Materials	ZX00		ZX10		ZX20	
	AC	DP-CFP	AC	DP-CFP	AC	DP-CFP
R_{sol} /Ω·cm^2	18.49	18.06	17.44	17.53	17.21	17.2
R_{ox} /Ω·cm^2	1273	1708	1285	2334	944.4	1142
CPE_{ox} /S·s^n·cm^{-2}	4.01×10^{-5}	1.88×10^{-5}	1.52×10^{-5}	1.75×10^{-5}	2.76×10^{-5}	1.85×10^{-5}
n_{ox}	0.86	0.89	0.92	0.92	0.91	0.91
R_{ct}. /Ω·cm^2	922.3	924.8	822.4	928.7	578.5	599.1
CPE_{dl} /S·s^n·cm^{-2}	1.87×10^{-3}	1.24×10^{-3}	1.36×10^{-3}	1.80×10^{-3}	2.85×10^{-3}	1.12×10^{-3}
n_{dl}	0.64	0.70	0.73	0.88	0.83	0.80

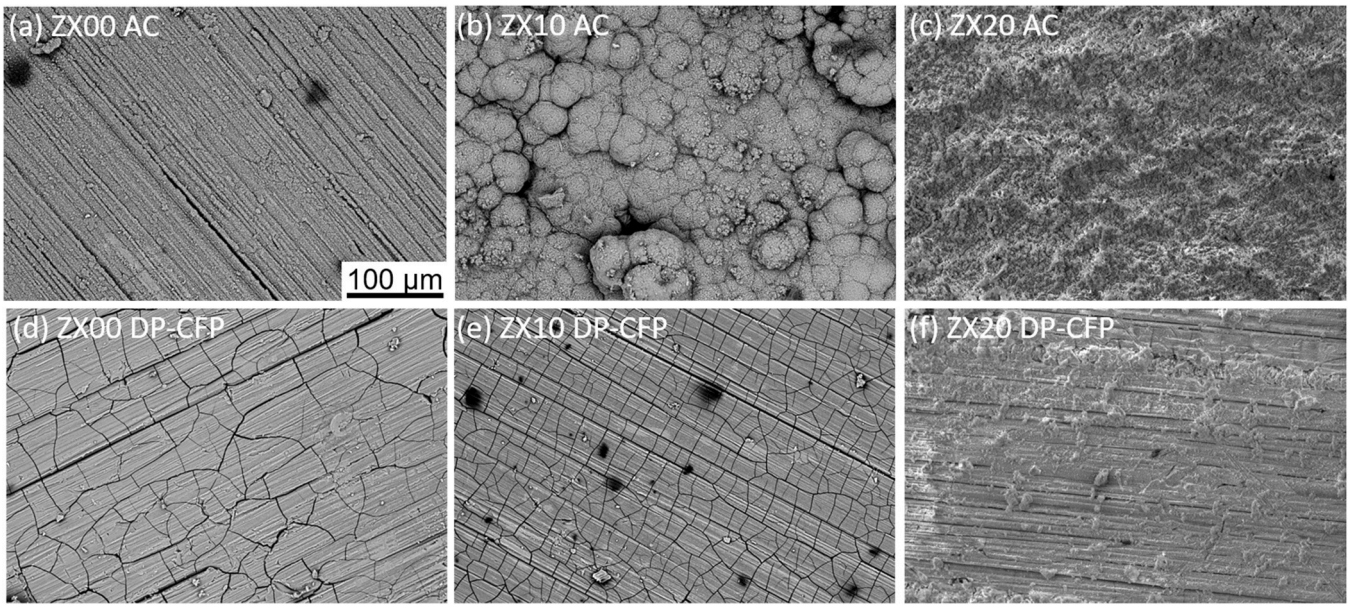

Fig. 7. Corrosion morphology with corrosion layer of as-cast (a) ZX00 alloy, (b) ZX10 alloy, (c) ZX20 alloy, and DP-CFPed (d) ZX00 alloy, (e) ZX10 alloy, (f) ZX20 alloy, after corrosion in stirring 0.9% NaCl solution for 3 days, obtained via SEM.

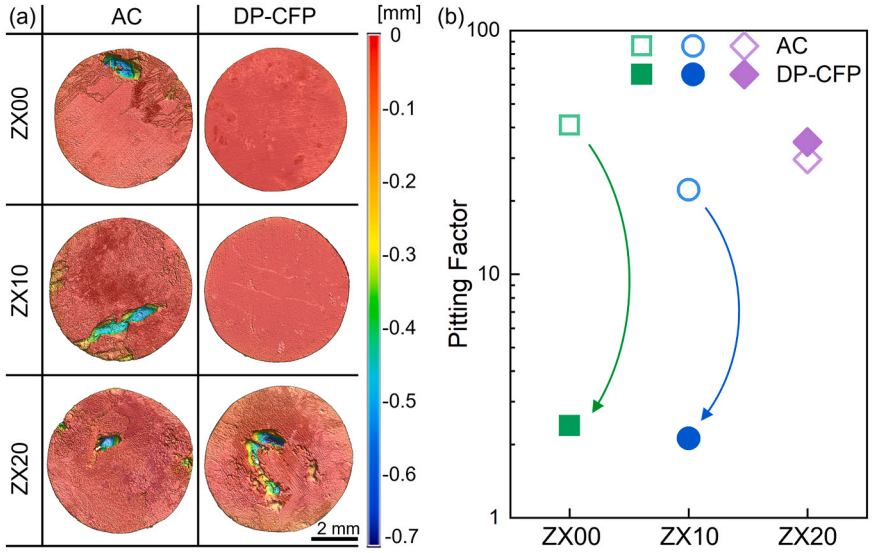

Fig. 8. (a) Corrosion morphology after removal of corrosion layer of as-cast and DP-CFPed ZX alloys and (b) corresponding pitting factor after corrosion in stirred 0.9% NaCl solution for 3 days by optical profilometer.

preferential sites for pitting initiation [39]. This usually leads to low corrosion resistance and inhomogeneous dissolution. The surface of the ZX alloys after corrosion is covered with corrosion products of varying rough morphology, see Fig. 7(a)-(c). In particular, the extent of corrosion product accumulation on the ZX10 and ZX20 samples is so pronounced that the grinding marks of the substrate are no longer visible, which indicates the thick porous $Mg(OH)_2$ layer, also reflecting low corrosion resistance. The surface of the underlying substrate exhibited a large number of grooves, see Fig. 9(a)-(c). The groove was located at α-Mg, while the secondary phase particles bulged at these grooves, indicating the cathodic nature of these Zn-rich phases. The chemical composition of the secondary particles was detected, indicating the disappearance of Mg_2Ca particles from the initial as-cast ZX00 and ZX10 alloys. In the as-cast ZX20 alloy, a network-like distribution of secondary phases with high zinc content was observed.

When DP-CFP was adopted, the corrosion surface of ZX20 after DP-CFP still exhibited pits and grooves, revealing similar corrosion rate of as-cast state. On the contrary, the corrosion surface of ZX00 alloy and ZX10 alloy after DP-CFP became flat, and no grooves were observed. As shown in Fig. 7(d) and (e), DP-CFPed ZX00 and ZX10 alloys exhibit a relatively flat corrosion surface with net-shaped cracks, which are attributed to volume shrinkage during the dehydration of the corrosion film. This morphology suggests the formation of a denser corrosion product layer, indicating better corrosion resistance [40]. The pitting factor of DP-CFPed ZX00 and ZX10 alloys decreased significantly to less than 3, as shown in Fig. 8(b), attributing to much more homogeneous dissolution. The surface of the substrate of DP-CFPed ZX00 and ZX10 alloys after corrosion appeared noticeably smoother and more uniform, see Fig. 9(d) and (e), and distribution of Zn and Ca was more homogeneous. This reduction in localized corrosion is crucial, as even minor localized attack can accelerate the deterioration of mechanical properties and lead to premature material failure. Therefore, the improved

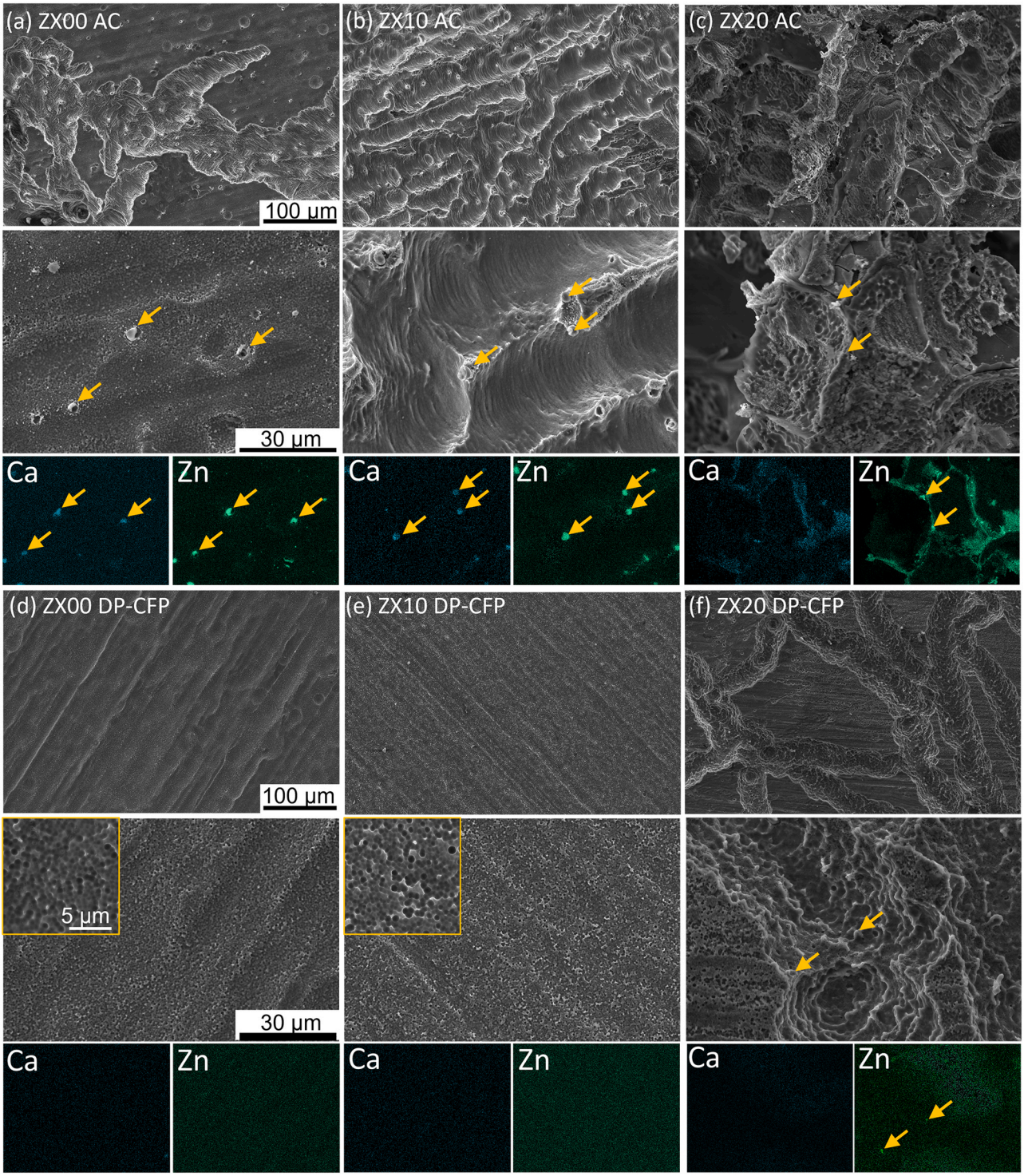

Fig. 9. Corrosion morphology without corrosion layer as well as its corresponding chemical composition distribution of as-cast (a) ZX00 alloy, (b) ZX10 alloy, (c) ZX20 alloy, and DP-CFPed (d) ZX00 alloy, (e) ZX10 alloy, (f) ZX20 alloy, after corrosion in stirring 0.9% NaCl solution for 3 days by SEM and EDS. Zn and Ca enriched particles were marked by yellow arrows.

resistance to localized corrosion provided by CFP represents a clear advantage in enhancing material durability.

Fig. 10 displays the cross-sectional morphology and the corresponding elemental distribution maps of different ZX alloys after immersion in a stirred 0.9% NaCl solution for 3 days. The as-cast ZX alloys exhibited an uneven interface between substrate and corrosion product, suggesting a significant degree of corrosion localization. Moreover, the corrosion product layers were comparatively thicker than those formed on the alloys processed with CFP. In contrast, the DP-CFPed ZX00 and ZX10 alloys revealed dense, uniform, and relatively flat corrosion products and respective interfaces, indicating a more uniform corrosion as compared to their as-cast counterparts. The average thickness of the corrosion product layer on DP-CFPed ZX10 alloy, about 5 μm, was lower than that of DP-CFPed ZX00 alloy, also reflecting the enhanced corrosion resistance of DP-CFPed ZX10 alloy in this study. In the case of ZX20 alloy, the corrosion products on DP-CFPed ZX20 alloy closely resembled

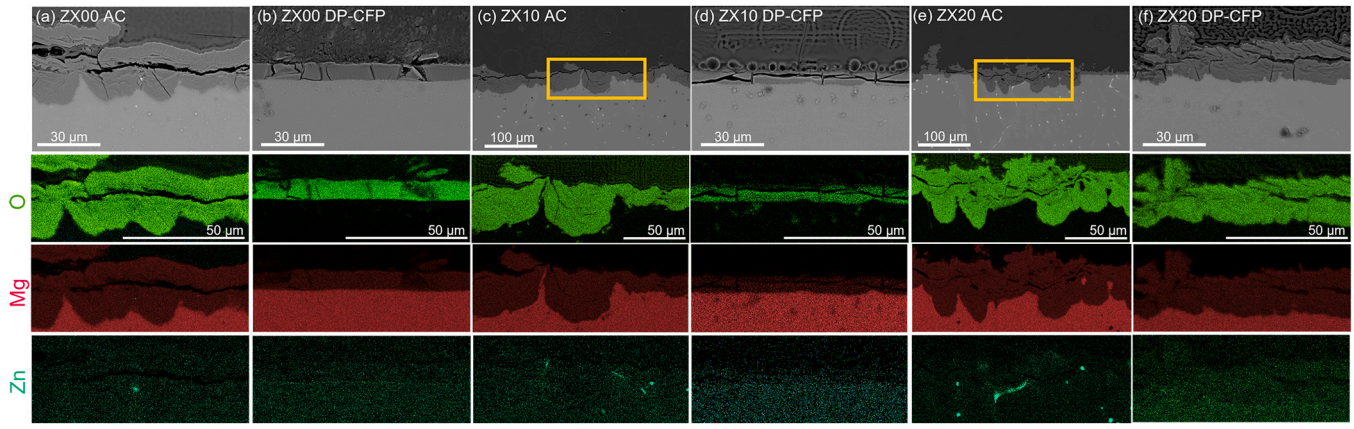

Fig. 10. Cross-section morphology as well as its corresponding chemical composition distribution of as-cast (a) ZX00 alloy, (b) ZX10 alloy, (c) ZX20 alloy, and DP-CFPed (d) ZX00 alloy, (e) ZX10 alloy, (f) ZX20 alloy, after corrosion in stirring 0.9% NaCl solution for 3 days by SEM and EDS.

those of the as-cast alloy, indicating a low corrosion resistance similar to the as-cast alloy.

4. Discussion

4.1. Secondary phase evolution during CFP

To understand the evolution of secondary phase particles during CFP with different heat inputs, the temperature history of the transition zone between TMAZ and SZ was measured via thermocouples, as shown in Fig. 11, since the evolution of the secondary phase is closely related to the thermal cycles. The processing parameters of SP-CFP with low heat input, i.e. with rotation speed of 1800 rpm, and high heat input, i.e. with rotation speed of 2400 rpm, were selected for analysis of secondary phase evolution. The type of secondary phases and the corresponding temperature are marked in Fig. 11 according to the equilibrium thermodynamic calculation, see Fig. S4. When ZX10 was processed under low heat input, the peak temperature during SP-CFP reached approximately 410 °C. This temperature falls within the phase region where only α-Mg and Mg_2Ca coexist. As a result, Mg_2Ca particles were retained in the final microstructure after cooling, as shown in Fig. 1(e_1). When ZX10 was processed with high heat input, the peak temperature during SP-CFP was about 470 °C, within the temperature range in which complete solid solution could be achieved, resulting in the final microstructure without observable secondary phase particle after cooling, see Fig. 1(f_1). Since the first plunge stage in DP-CFP used the same processing parameters as SP-CFP under high heat input, it is inferred that a complete solid solution was achieved during this stage, and no secondary phases formed in the subsequent stages, see Fig. 1(g_1).

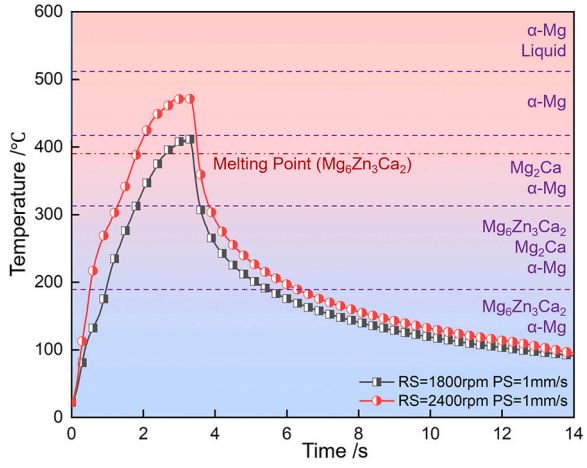

Fig. 11. Thermal cycles during SP-CFP with different heat inputs on ZX10 alloy. The type of phase and corresponding temperature from equilibrium thermodynamic calculations from Fig. S4 are also indicated.

Typically, the brief thermal exposure during conventional rapid heating is inadequate for establishing equilibrium microstructures at peak temperatures, as diffusion-controlled transformations require longer times. For example, normal heat treatment for solid solution usually takes more time (several hours) [41,42]. In contrast, CFP can significantly refine the secondary phases and even achieve complete solid solution within a few seconds. This remarkable acceleration of phase transformation suggests that near-equilibrium states can be attained rapidly, likely due to enhanced dissolution kinetics of secondary phase particles under severe plastic deformation. The 'stop-action' technique was carried out on CFP with different processing parameters to investigate the evolution of secondary phase. The "frozen" transition zone from BM to the processed rod, marked as region *I* in Fig. S3, was characterized by SEM with EDS, as shown in Fig. 12.

According to our previous work on material flow behavior during CFP [22], the material in the TMAZ is subjected to a very low level of strain. As the shoulder begins to plunge, the material located at the front of the SZ, adjacent to the TMAZ, undergoes intense shear deformation with a relatively high shear strain rate. As the plunging continues, this region is transported deeper into the SZ, where its rotational speed gradually approaches that of the tool and eventually synchronizes with it, resulting in a reduction in shear strain rate. Based on these three distinct stages characterized by different strain rates, the investigation of microstructure evolution can be correspondingly divided into three regions: the TMAZ, the front of the SZ, and the inner SZ within the rod. The characteristics of the secondary phase in these three regions were investigated to understand the evolution of the secondary phase of ZX10 alloy during CFP, as shown in Fig. 12(b-d).

The TMAZ was divided into 2 parts, i.e. TMAZ-I and TMAZ-II, according to the characteristics of the secondary phase. In TMAZ-I near BM, the distribution, shape, and size of the secondary phase were similar to those in the BM. TMAZ-II, located close to the SZ, exhibited for low heat input elongated network-shape second phase distributed at grain boundaries, see Fig. 12(d_1), as well as elliptical second phase particles. EDS was carried out to distinguish the components of these two types of secondary phases. Fig. 13 displays the distribution of Zn and Ca contents near the interface between SZ and TMAZ-II, marked as A in Fig. 12(a_1). According to EDS results, the second phase particles with higher Ca content were Mg_2Ca particles, while the irregular network-like second phase distributed at grain boundaries was $Mg_6Zn_3Ca_2$. The distribution of $Mg_6Zn_3Ca_2$ along the recrystallized grain boundaries suggests that it melted and penetrated into these regions, as the processing temperature exceeded its relatively low melting point. Similar observations of

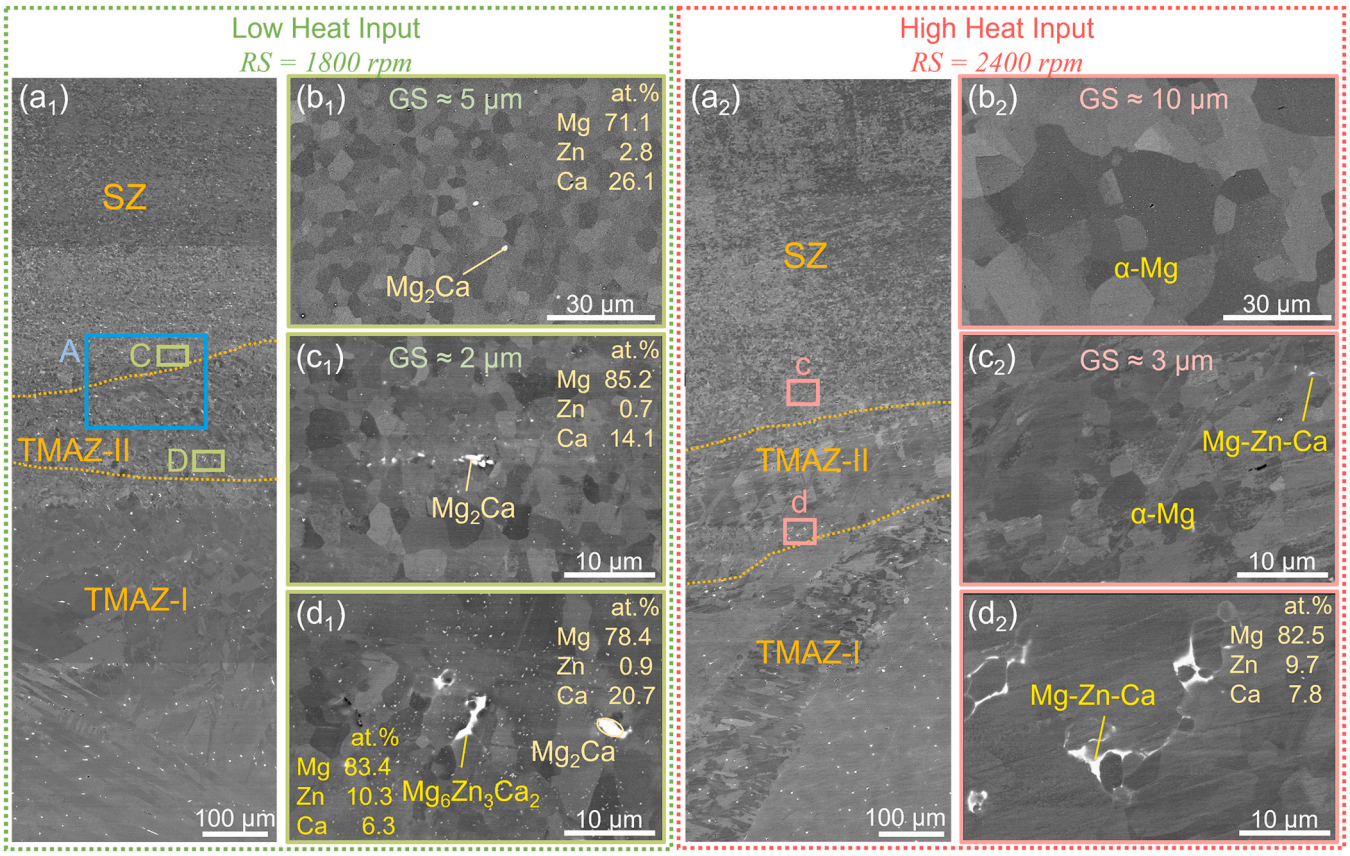

Fig. 12. Microstructure of transition zone between SZ and TMAZ of ZX10 alloy obtained via "stop-action" experiment on CFP with (a_1) low and (a_2) high heat input. (b_1) SZ in rod obtained with low heat input, (c_1) SZ front marked as C region in (a_1), (d_1) TMAZ marked as D region in (a_1). (b_2) SZ in rod obtained with high heat input, (c_2) SZ front marked as c region in (a_2), (d_2) TMAZ front marked as d region in (a_2).

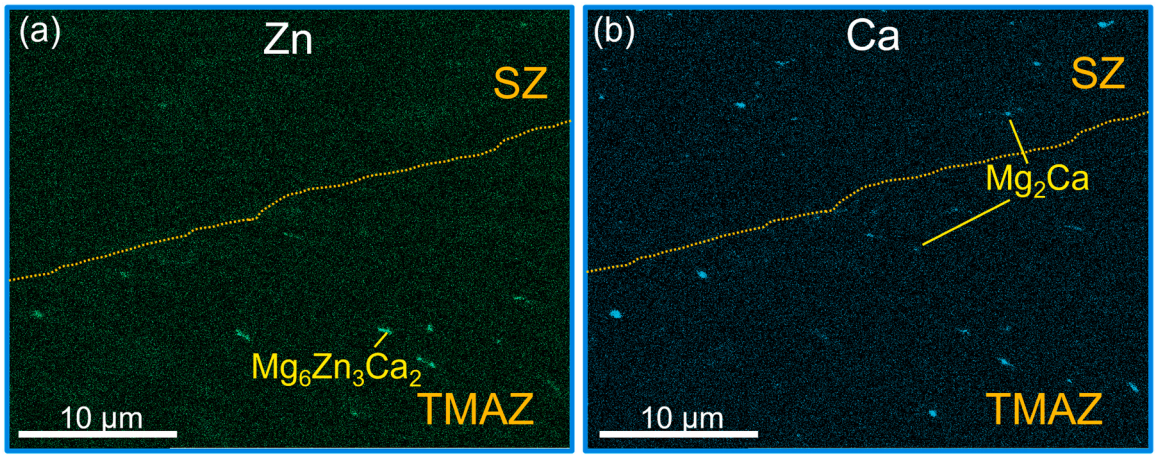

Fig. 13. Distribution of Zn and Ca contents near the interface between SZ and TMAZ of ZX10 alloy processed with low heat input, marked as A in Fig. 11(a_1).

partially melted, network-like phases along grain boundaries during severe plastic deformation have also been reported in [42]. In contrast, the morphology and size of Mg_2Ca remained unchanged, which can be attributed to its higher thermal stability [43]. In the SZ, the elongated network-shape second phase with enrichment of Zn and Ca disappeared, and Zn distributed uniformly, see Fig. 12(a_1) and Fig. 13, indicating the complete solid solution of Zn content. At the same time, the initial large Mg_2Ca phase was broken into smaller particles due to the severe shear deformation, see Fig. 12(c_1), and the final microstructure in the processed rod exhibited refined elliptical Mg_2Ca particles. When higher heat input was adopted, TMAZ-II exhibited an elongated network-shape Mg-Zn-Ca phase, but no Mg_2Ca particles were observed, see Fig. 12(a_2) and Fig. 12(d_2). In the front of SZ near the interface, the volume of Mg-Zn-Ca decreased significantly, and there was no observable secondary phase in the final processed rod.

The evolution of the secondary phase of ZX10 alloy during CFP with different heat inputs is displayed in Fig. 14. During CFP with low heat input, hot deformation in the region around the $Mg_6Zn_3Ca_2$ phase promotes particle-stimulated nucleation (PSN) near the secondary particles, resulting in the formation of fine recrystallized grains [22]. As the

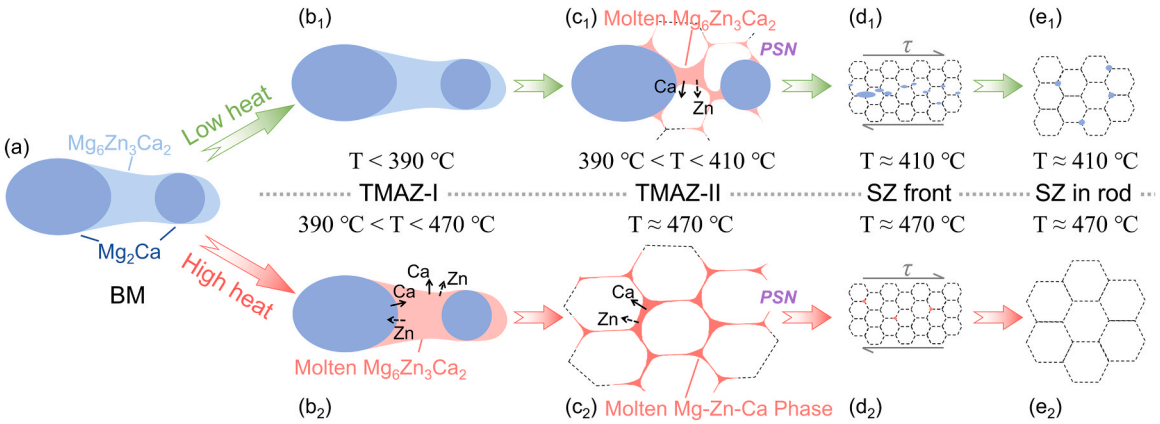

Fig. 14. Secondary phase evolution during CFP with different heat inputs.

processing temperature in TMAZ-II reaches 390 °C, exceeding the melting point of $Mg_6Zn_3Ca_2$, this phase begins to melt (see Fig. 14(c_1)). The molten $Mg_6Zn_3Ca_2$ penetrates into the recrystallized grain boundaries, significantly increasing the interface area between the liquid phase and α-Mg. According to the calculated equilibrium phase at this temperature, $Mg_6Zn_3Ca_2$ is not stable and tends to dissolve into α-Mg, and the enlarged interface area accelerates the diffusion of Zn and Ca from the molten $Mg_6Zn_3Ca_2$ into α-Mg. As processing advances, the local temperature at the front of the SZ increases to about 410 °C, accompanied by intense plastic shear deformation in this region, see Fig. 14(d_1). The melting of $Mg_6Zn_3Ca_2$ at grain boundaries is dispersed due to the high shear strain rate and the extensive recrystallization, further accelerating the diffusion of Zn and Ca, resulting in complete solid solution of $Mg_6Zn_3Ca_2$ phase. At the same time, the solid Mg_2Ca particles break into fine particles due to severe shear deformation. The fracture of the secondary phase during severe plastic deformation has also been reported in [24,44,45]. At the interior of the SZ, see Fig. 14(e_1), the decreasing shear strain rate leads to static recrystallization and grain growth. At the same time, the refined Mg_2Ca particles still exist and spheroidizes, since the Mg_2Ca phase is stable at 410 °C. During CFP with high heat input, the $Mg_6Zn_3Ca_2$ phase melts already in the TMAZ-I at a temperature higher than 390 °C, see Fig. 14(b_2). As processing time increases and temperature rises, the Zn diffuses from the melting $Mg_6Zn_3Ca_2$ phase to the Mg_2Ca phase and α-Mg, and the Ca diffuses from the Mg_2Ca phase to the melting $Mg_6Zn_3Ca_2$ phase, resulting in the melting Mg-Zn-Ca phase. This melting Mg-Zn-Ca phase is not the equilibrium phase in the whole system at this temperature and tends to dissolve into α-Mg. In TMAZ-II at a higher temperature, i.e. about 470 °C, the melting Mg-Zn-Ca phase penetrates into recrystallized grain boundaries, see Fig. 14(c_2), and the diffusion of Zn and Ca from Mg-Zn-Ca phase to α-Mg accelerates. The liquid Mg-Zn-Ca phase is further dispersed due to the high shear strain rate at the front of SZ, accelerating the formation of a complete solid solution, see Fig. 14(d_2). During the subsequent static recrystallization and grain growth within the interior of the SZ, see Fig. 14(e_2). The absence of secondary phases in the final microstructure indicates that a complete solid solution was achieved and maintained, corresponding to the equilibrium state at 470 °C. In summary, the severe shear deformation as well as the extensive recrystallization during CFP significantly accelerate the solid solution of melting phases during processing and refinement of the hard secondary phase.

4.2. Corrosion mechanism

To further understand the significant improvement of corrosion resistance of ZX10 alloy after CFP in NaCl solution, the corrosion mechanisms of as-cast ZX10 alloy and DP-CFPed ZX10 alloy were further investigated. When Mg alloys are exposed to NaCl solution, Mg undergoes an anodic reaction (1) first, as:

$$Mg\ (s) \rightarrow Mg^{2+}(aq) + 2e^- \quad (1)$$

In the meantime, the dominant cathodic water reduction reaction (2) occurs, as:

$$2H_2O\ (l) + 2e^- \rightarrow 2OH^-(aq) + H_2(\uparrow) \quad (2)$$

Cathodic oxygen reduction reaction (3) also occurs, as:

$$O_2\ (g) + 2H_2O\ (l) + 4e^- \rightarrow 4OH^-(aq) \quad (3)$$

Subsequently, the main corrosion product, magnesium hydroxide $Mg(OH)_2$, is formed by reaction (4) and accumulates on the surface of the Mg alloys.

$$Mg^{2+}(aq) + 2OH^-(aq) \rightarrow Mg(OH)_2(s) \quad (4)$$

To clarify how secondary phases in as-cast ZX10 alloy evolve during corrosion in NaCl solution, the characteristics of the secondary phases were compared in three conditions: within the corrosion product (Fig. 15(a)), at the corrosion product/substrate interface (Fig. 15(b)), and in the pre-corrosion specimens (Fig. S5). This comparative analysis highlights the chemical evolution and redistribution of secondary phase constituents, offering insight into their role in the corrosion mechanism of ZX10 alloy. The spherical secondary phase in as-cast ZX10 alloy consists of two components, the lighter part in SEM with higher Zn content is the $Mg_6Zn_3Ca_2$ phase, and the darker part with higher Ca content is the Mg_2Ca phase, see Fig. S5. After immersion in NaCl solution, the Ca content in the secondary phase embedded into the corrosion products decreased and disappeared, while the Zn content remained high, see Fig. 15(a), indicating that the Ca selectively dissolves from the secondary phase dissolved into the corrosion medium during immersion after the particle loses the electrical contact with Mg-matrix. The interface between the substrate and corrosion product displays localized galvanic corrosion at the secondary phase particle, see Fig. 15(b). At position A, which was identified as the original location of the Mg_2Ca phase based on the as-cast secondary phase distribution (Fig. S5), this phase had disappeared and was replaced by an oxygen-rich corrosion product. In contrast, the neighboring $Mg_6Zn_3Ca_2$ phase showed no signs of corrosion-induced alteration. The other secondary phase at B, closer to the surface, exhibited higher Zn content, while Ca disappeared, indicating the selective dissolution of Ca and Mg from the $Mg_6Zn_3Ca_2$ phase and the formation of the Zn-enriched phase, which has also been reported by Cihova et al. [46].

After CFP processing, Zn in the secondary phase of ZX00 and ZX10 alloys dissolved and uniformly distributed in α-Mg, eliminating micro-galvanic corrosion and leading to uniform corrosion with high corrosion resistance, as shown in Fig. 10. Comparing the corrosion behavior of DP-CFPed ZX00 and ZX10 alloys, both free of secondary phase, DP-CFPed ZX10 alloy exhibited higher corrosion resistance since the

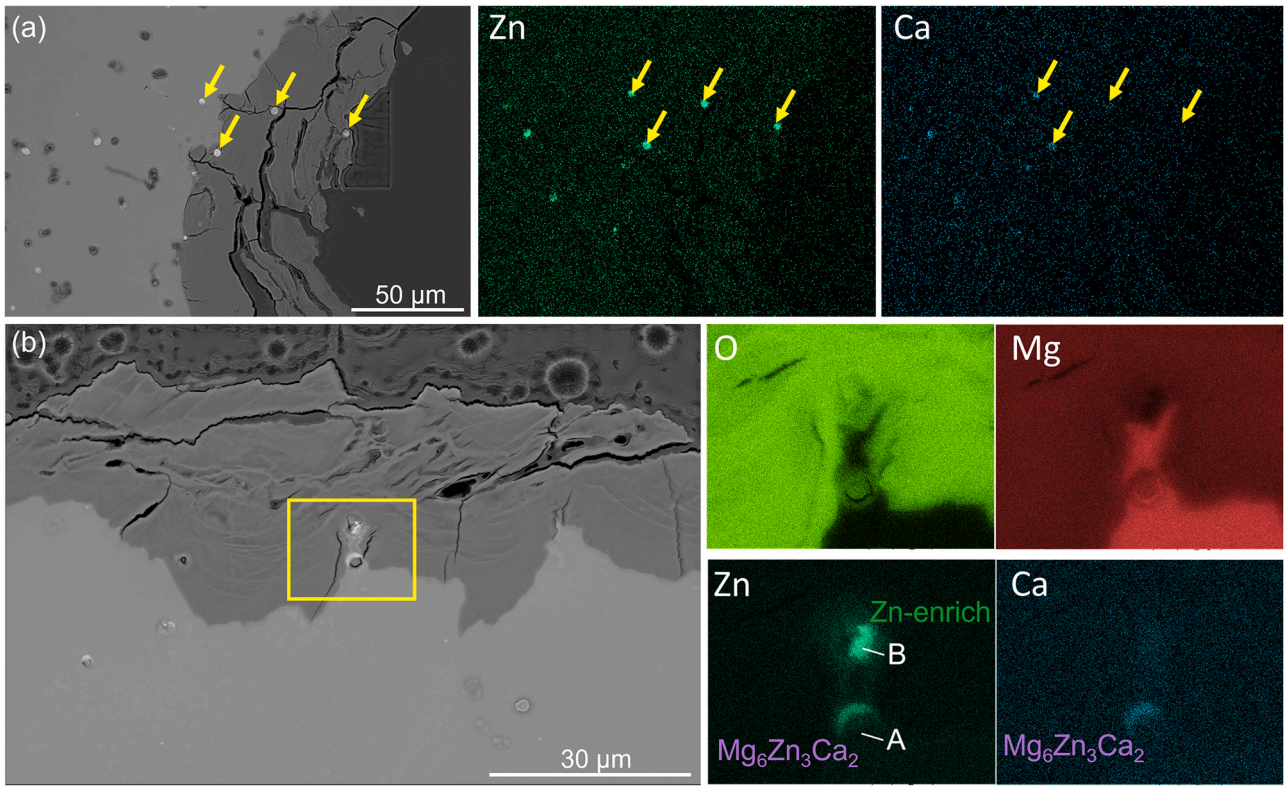

Fig. 15. Secondary phases after corrosion, characterized by SEM and EDS. (a) Secondary phase and corresponding Zn and Ca distribution of as-cast ZX10 alloy after immersion in 0.9% NaCl for 3 days. (b) Secondary phase at the interface between Mg substrate and corrosion product.

surface oxide/hydroxide films on DP-CFPed ZX10 alloy exhibited better barrier properties, according to the EIS results. To understand the effect of Zn content in α-Mg on the corrosion product and the resultant corrosion resistance, the interface between α-Mg and the corrosion product was characterized by SEM with EDS, see Fig. 16. The interface between α-Mg and corrosion products exhibited a continuous layer with brighter contrast in backscattered electron (BSE) mode of SEM, enriched with Zn element. The continuous layer enriched by the Zn element on the surface of the Mg substrate has also been reported in Mg-Zn-based alloys after immersion [40,47,48].

The accumulation of Zn at the interface was further characterized by TEM, as shown in Fig. 17. Based on image contrast and distribution of porosity, the corrosion product layer formed on the surface of the CFPed ZX10 alloy can be roughly divided into four distinct regions (Region I-IV), see Fig. 17(a) and (b). Region I appears as a series of parallel, elongated strip-like structures with a highly porous and loose morphology. Region II surrounds Region I and exhibits slightly reduced porosity compared to Region I. Regions III and IV form layered structures covering the surface of the Mg alloy substrate. Among them, Region III is also porous, while Region IV is relatively dense and compact. Importantly, Region IV forms a continuous and uniform layer that fully covers the underlying Mg substrate. Based on its compactness and integrity, Region IV is considered to play a dominant role in isolating the corrosive environment and providing corrosion protection for the underlying Mg substrate. According to EDS analysis, see Fig. 17(c) and (d), Regions I through III are mainly composed of Mg and O. TEM selected area electron diffraction (SAED) patterns and high-resolution TEM (HRTEM) images, as shown in Fig. 17(e)-(h), further reveal that these regions consist predominantly of amorphous material and crystalline MgO, with Region III showing a higher degree of crystallinity than Regions I and II. In the dense and continuous Region IV, a significant enrichment of Zn element, other than Mg and O, was observed. HRTEM imaging confirms that this region is primarily amorphous, see Fig. 17(i). In typical Zn-free magnesium corrosion environments, the surface

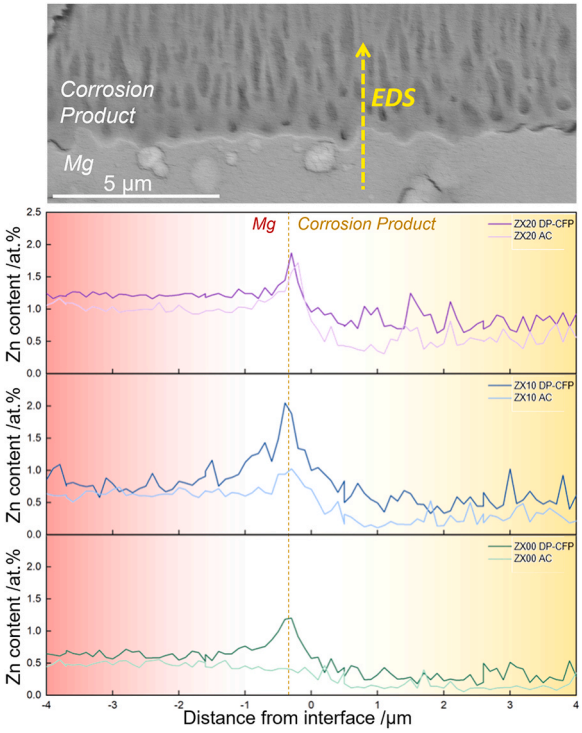

Fig. 16. Distribution of Zn content measured by EDS from the α-Mg in the substrate to the corrosion products in as-cast and DP-CFPed ZX00, ZX10, and ZX20 alloys. The SEM image shown corresponds to the DP-CFPed ZX10 alloy.

corrosion layer generally consists of crystalline MgO [49]. However, when Zn-ions are enriched beyond a certain threshold, it can induce

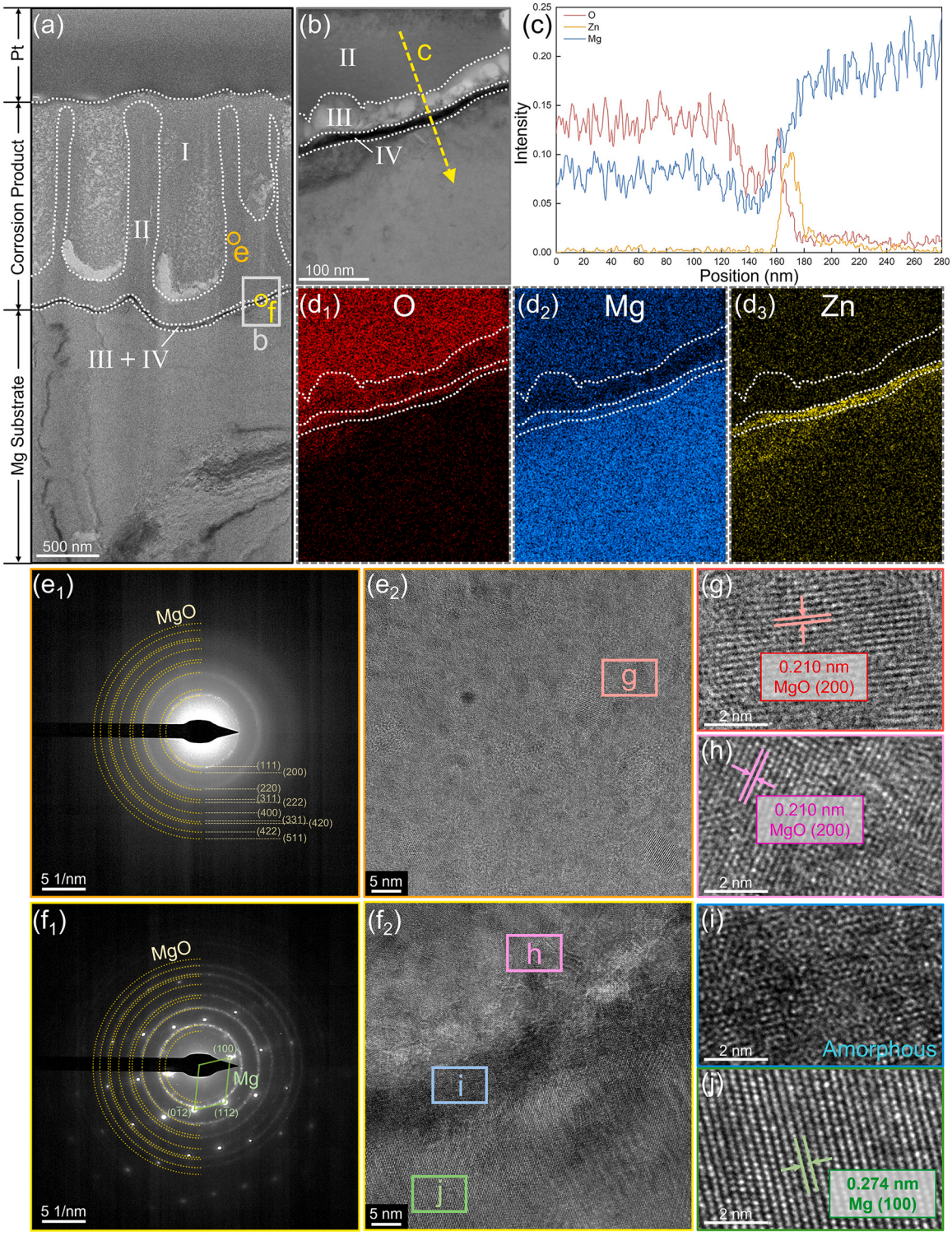

Fig. 17. (a) Bright-field (BF) TEM image showing the cross-sectional morphology of the corrosion product film. (b) Enlarged BF image of the interface between the corrosion product and the underlying Mg substrate, corresponding to region b in (a). (c) Elemental line scan along the line marked c in (b), illustrating the chemical composition distribution across the interface. (d_1–d_3) Elemental mapping of the same region shown in (b), highlighting the distribution of O, Mg and Zn elements. (e_1) Selected area electron diffraction (SAED) pattern from region e in (a), and (e_2) corresponding high-resolution TEM (HRTEM) image. (f_1) SAED pattern from region f in (a), and (f_2) corresponding HRTEM image. (g–j) Enlarged views of the regions marked g–j in (e_2) and (f_2), showing detailed lattice structures.

lattice distortions and increase the density of defects in MgO. These structural distortions and internal strain reduce the long-range order of the crystal lattice, promoting the formation of amorphous domains [50]. Previous studies have shown that amorphous structures generally offer superior corrosion resistance due to the absence of defects compared to crystalline phases [51,52]. Therefore, the dense, continuous, and Zn-rich amorphous corrosion layer in Region IV is believed to serve as an effective barrier that protects the underlying Mg substrate. This is also supported by the EIS results, which demonstrate significantly higher impedance values, indicating improved corrosion resistance. In

comparison with DP-CFPed ZX00 alloy, the accumulation of Zn-rich corrosion products at the surface of the DP-CFPed ZX10 alloy substrate was more significant, see Fig. 16, resulting in better barrier properties and corrosion resistance.

The onset of corrosion process of as-cast and DP-CFPed ZX10 alloy in NaCl solution is summarized in Fig. 18. The as-cast ZX10 alloy exhibits both Mg_2Ca and $Mg_6Zn_3Ca_2$ phases. It has been reported that the Mg_2Ca phase exhibits more negative potential compared to Mg [15,53], while the $Mg_6Zn_3Ca_2$ phase exhibits a more positive potential [54]. Therefore, during immersion of as-cast ZX10 alloy, the Mg_2Ca phase acts as an anode and dissolves preferentially to α-Mg, see Fig. 18(a_1), also evident in SEM micrographs, Figs. 9 and 15. Subsequently, the $Mg_6Zn_3Ca_2$ phase acts as cathodic site and leads to the anodic dissolution of α-Mg, see Fig. 18(a_2). As corrosion progresses, the $Mg_6Zn_3Ca_2$ phase on the surface of the substrate continuously acts as the cathode, causing continuous and rapid corrosion of α-Mg with loose spongy MgO/$Mg(OH)_2$ product films due to micro-galvanic corrosion, see Fig. 18(a_3). At the same time, Zn in the $Mg_6Zn_3Ca_2$ phase is cathodically protected through polarization by the actively corroding α-Mg matrix. Ca and Mg, in contrast, preferentially dissolve, leading to Zn enrichment in the secondary phase. Similar dealloying of Ca and Mg in a MgZnCa intermetallic phase has been reported in [46]. The resulting enrichment of Zn, concomitant with the ennoblement of the secondary phase, renders the secondary phase even more effective cathodic spots, provoking severe localized micro-galvanic corrosion and deterioration of the global corrosion resistance. Such micro-galvanic interactions between the α-Mg matrix and the secondary phases may serve as preferential sites for the initiation of localized pitting, which could subsequently contribute to the broader localized corrosion of the alloy [55]. When the secondary phase is separated from the α-Mg substrate, see Fig. 18(a_4), the loss of direct electrical contact between the α-Mg substrate and the secondary phase eliminates the micro-galvanic corrosion. After detachment, any residual Mg and Ca retained within the intermetallic phase continue to undergo preferential oxidation relative to Zn, leading to a progressive Zn enrichment in the isolated particles. This behavior is reflected by the gradual disappearance of Ca from detached intermetallics embedded within the corrosion products, as shown in Fig. 15(a). The farther these particles are located from the substrate and the longer they have been exposed to the electrolyte, the more pronounced the Ca depletion becomes. Such selective dissolution of Mg and Ca from Zn-rich intermetallics, once decoupled from the substrate, is referred to as kinetic dealloying [46].

In comparison, the secondary phase in DP-CFPed ZX10 completely solidly dissolves into the α-Mg, and α-Mg exhibits a uniform distribution of Zn with higher content, see Fig. 18(b_1). Due to the different dissolution tendencies of the alloying elements, Mg and Ca dissolve preferentially as Mg^{2+} and Ca^{2+}, followed by dissolution of Zn, forming Zn^{2+} ions. No micro-galvanic corrosion occurs due to the homogeneous microstructure, leading to a uniform and flat surface of the substrate and denser MgO/$Mg(OH)_2$ product, see Fig. 18(b_2). As the corrosion progresses, the concentration of Zn^{2+} in the media increases as Zn gradually dissolves from the alloy. $Zn(OH)_2$ possesses an extremely low solubility product ($K_{sp} \approx 3 \times 10^{-17}$), much lower than that of $Mg(OH)_2$ ($K_{sp} \approx 5.61 \times 10^{-12}$) and $Ca(OH)_2$ ($K_{sp} \approx 5.02 \times 10^{-6}$) [56]. Even when the Zn^{2+} concentration in the media is relatively low, Zn ions readily precipitate as $Zn(OH)_2$ at the alkaline interface. Due to the relatively high concentration of Mg^{2+} ions, they also contribute to the formation of $Mg(OH)_2$, and together with the Zn-containing species, co-deposit to form a continuous amorphous Mg-Zn-O/OH layer at the alloy surface, where Mg and Zn are present in the divalent state, see Fig. 18(b_3) and (b_4). The enrichment of Zn element at the interface between the Mg substrate and the MgO layer has also been widely reported in Zn-containing Mg alloys after corrosion [57–59]. Unocic et al. [58] suggested that Zn segregation may hinder the outward diffusion of Mg ions during film growth, thereby leading to a denser and more protective surface film compared with ultra-high-purity Mg. Consistent with these findings, the Zn-enriched amorphous Mg-Zn-O/OH layer observed in this study serves as an effective barrier, enhancing its corrosion resistance.

ZX10 alloys after CFP with different processing parameters exhibited similar corrosion resistance. The main difference between SP-CFPed ZX10 alloy with low heat input and DP-CFPed ZX10 alloy was the secondary phase. SP-CFPed ZX10 alloy with low heat input exhibited fine Mg_2Ca particles, while DP-CFPed ZX10 alloy achieved complete solid solution, indicating that the fine Mg_2Ca particles did not strongly affect the corrosion resistance. The main reason is that the fine anodic Mg_2Ca particles with low volume corroded preferentially and would not further aggravate the micro galvanic corrosion of α-Mg. The main difference between SP-CFPed ZX10 alloy with high heat input and DP-CFPed ZX10 alloy was the grain size. The grain size of SP-CFPed ZX10 alloy with high heat input (about 10 μm) was much larger than that of DP-CFPed ZX10 alloy (about 5 μm), illustrating the grain size is not an important factor affecting the corrosion rate.

The Zn content strongly affects the type and volume of the secondary phase in ZX alloys. As the Zn content increased from 0.5% to 2.0 wt% in

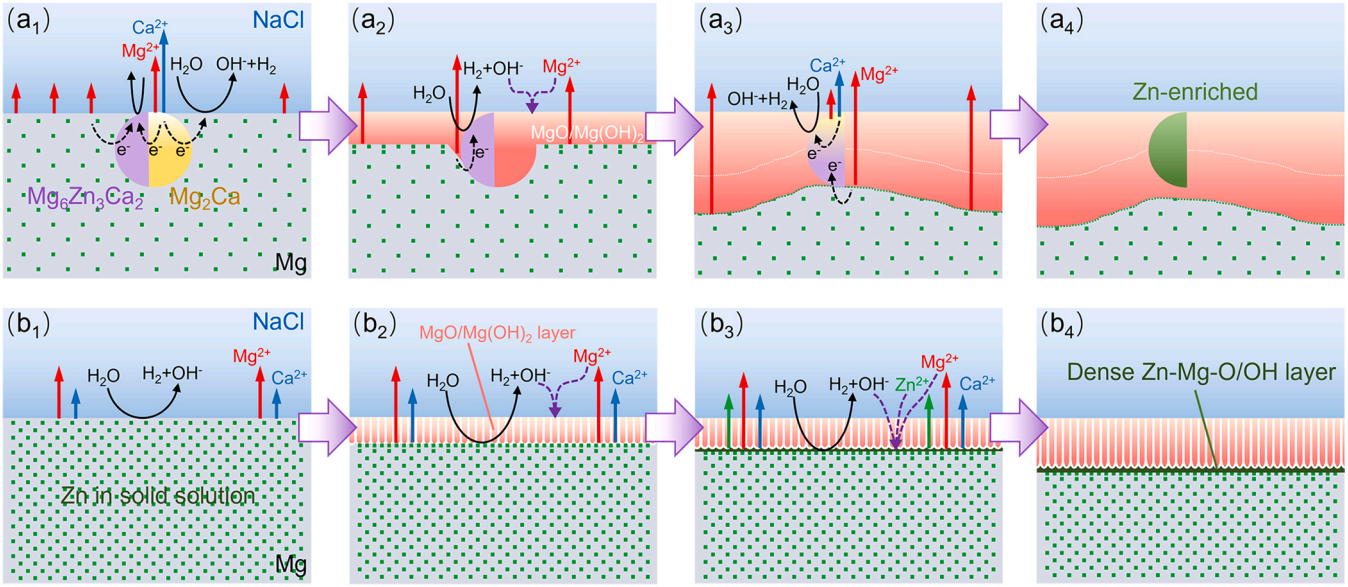

Fig. 18. Corrosion procedure and mechanism of (a) as-cast and (b) DP-CFPed ZX10 alloy in NaCl solution.

as-cast ZX alloys, the volume of the cathodic secondary phase increased, leading to the enhancement of localized galvanic corrosion and lower corrosion resistance. In the case of CFPed ZX alloys, appropriately increasing the zinc content, from 0.5 wt% to 1.0 wt%, is beneficial to form a protective Zn-rich amorphous layer, on the surface of underlying Mg substrate, which possibly accounts for its higher corrosion resistance. When the Zn content reaches 2.0 wt%, secondary phase with Zn enrichment was detected in the grooves on the corroded surface, see Fig. 9(f), indicating that the enrichment of Ca and Zn at grain boundaries led to micro-galvanic corrosion and higher corrosion rate compared to DP-CFPed ZX00 and ZX10 alloys.

4.3. Advantages and prospects of CFP

To further assess the corrosion performance and potential applicability of the CFP-treated ZX alloy, the corrosion rate of the DP-CFPed ZX10 alloy, which exhibits the highest corrosion resistance among the alloys investigated in this work (Fig. 4), was evaluated in static 3.5 wt% NaCl solution, a standard medium commonly employed for corrosion rate measurements, for 30 days. The corrosion behavior was quantified using both hydrogen evolution and mass loss method, yielding corrosion rates of 0.20 mm/yr and 0.16 mm/yr, respectively. In comparison with other rare-earth-element free (REE-free) Mg alloys reported in the literature [38,48,60–74], as shown in Fig. 19, the CFP ZX10 alloy demonstrates superior corrosion resistance, even surpassing that of high-purity magnesium (about 0.3 mm/yr). Although micro-alloyed Mg-Ca systems can achieve slightly lower corrosion rates (approximately 0.1 mm/yr), such performance is generally limited to the as-cast condition, where mechanical properties remain inadequate, with yield strength of 64 MPa and elongation of 4.4% [60]. Upon heat treatment or thermomechanical processing to enhance mechanical strength, their corrosion resistance typically deteriorates, primarily due to the precipitation of Fe-containing intermetallic phases that act as micro-galvanic sites [38]. In contrast, the CFP ZX10 alloy maintains a favorable combination of corrosion resistance and mechanical performance, underscoring the effectiveness of the CFP process in simultaneously optimizing both properties. These results suggest that the CFP ZX10 alloy possesses considerable potential for advanced structural applications, where a combination of high mechanical integrity and corrosion resistance is required. In addition, Mg-Zn-Ca alloys are well suited for biomedical implant applications due to the relatively high toxicity limits of Zn and high biocompatibility of Ca and Mg.

5. Conclusion

In this study, the microstructure, especially the secondary phase, as well as the corrosion behavior of Mg-Zn-Ca alloys produced by constrained friction processing technique were characterized. The secondary phase evolution was revealed based on the analysis of “stop-action” samples. Additionally, to understand the effects of the secondary phase and corrosion mechanism, the corrosion product on different ZX alloys after immersion was characterized. The following conclusions are obtained:

(a) During CFP, when the temperature exceeds the melting point of $Mg_6Zn_3Ca_2$, the phase melts and penetrates into recrystallized grain boundaries, increasing the interface area with α-Mg and accelerating Zn and Ca diffusion into the matrix.
(b) Severe shear deformation and extensive recrystallization during CFP disperse the molten phase and fragment the solid Mg_2Ca particles, greatly increasing the dissolution rate of secondary phases. This process rapidly reduces the secondary phase fraction and can even achieve a complete solid solution within a short processing time.
(c) The corrosion resistance of ZX00 and ZX10 alloys after CFP in NaCl solution increases due to the decrease of micro-galvanic corrosion at the secondary phase and generated uniform dense corrosion product. The pitting factor significantly decreased by approximately one order of magnitude after CFP, confirming a substantial reduction in localized corrosion. CFPed ZX00 and CFPed ZX10 alloys without observable secondary phases exhibit better corrosion resistance.
(d) CFPed ZX10 alloy exhibits the best corrosion resistance in NaCl solution in this study. Compared with CFPed ZX00, accumulation of Zn-containing continuous corrosion layer possibly contributes to the improvement of the barrier property of surface corrosion product films.

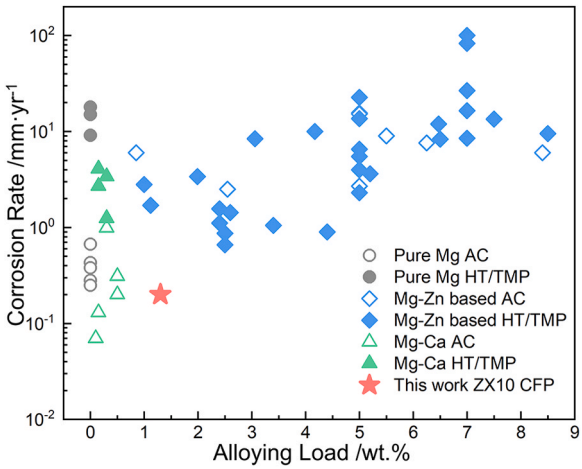

Fig. 19. Comparison of the corrosion rate of the DP-CFPed ZX10 alloy with reported rare-earth-element-free (REE-free) Mg alloys [38,48,60–74], including pure Mg, Mg–Zn-based, and Mg–Ca alloys, in both as-cast and heat-treated/thermo-mechanical processed (HT/TMP) conditions, as a function of total alloying content. The corrosion rates were determined from weight loss measurements obtained in standard static 3.5 wt% NaCl immersion tests.

CRediT authorship contribution statement

Banglong Fu: Writing – review & editing, Validation, Funding acquisition. **Benjamin Klusemann:** Writing – review & editing, Supervision, Funding acquisition. **Ting Chen:** Writing – review & editing, Writing – original draft, Visualization, Methodology, Investigation, Formal analysis, Data curation, Conceptualization. **Jean Pierre Bergmann:** Writing – review & editing, Supervision. **Mikhail L. Zheludkevich:** Writing – review & editing. **Jorge F. dos Santos:** Supervision, Project administration. **Sviatlana V. Lamaka:** Writing – review & editing, Methodology, Investigation. **Emad Maawad:** Methodology. **Tong Shen:** Writing – review & editing, Investigation. **Yulong Wu:** Writing – review & editing, Validation, Methodology, Investigation. **Uceu F.H.R. Suhuddin:** Writing – review & editing, Methodology. **Bahram Vaghefinazari:** Writing – review & editing, Methodology, Investigation.

Declaration of Competing Interest

The authors declare that they have no known competing financial interests or personal relationships that could have appeared to influence the work reported in this paper.

Acknowledgments

Mr. Ting Chen and Mr. Yulong Wu thank the China Scholarship Council for the award of fellowship and funding (No. 202006230137, No. 202106050030). Dr. Banglong Fu acknowledge the financial support of the National Natural Science Foundation of China (Grant No.

52405386), State Key Laboratory of Precision Welding & Joining of Materials and Structures (Grant No. MSWJ-24M13) and "Project 2025HWYQ-005 supported by Shandong Provincial Natural Science Fund for Excellent Young Scientists Fund Program (Overseas)". We acknowledge DESY (Hamburg, Germany), a member of the Helmholtz Association HGF, for the provision of experimental facilities. Parts of this research were carried out at PETRA III. The authors are grateful to Mr. Günter Meister Institute of Metallic Biomaterials and Mr. Gert Wiese Institute of Surface Science of Helmholtz-Zentrum Hereon, for the provision of the base materials used in this study and the guidance of the metallographic preparation. The technical support of Mr. Menno Peters, from Helmholtz-Zentrum Hereon, Institute of Material and Process Design during this work is gratefully acknowledged.

Appendix A. Supporting information

Supplementary data associated with this article can be found in the online version at doi:10.1016/j.corsci.2026.113819.

Data availability

No data was used for the research described in the article.

References

[1] E. Ghali, W. Dietzel, K.-U. Kainer, General and localized corrosion of magnesium alloys: a critical review, J. Mater. Eng. Perform. 13 (1) (2004) 7–23, https://doi.org/10.1361/10599490417533.
[2] B. Liu, J. Yang, X. Zhang, Q. Yang, J. Zhang, X. Li, Development and application of magnesium alloy parts for automotive OEMs: A review, J. Magnes. Alloy 11 (1) (2023) 15–47, https://doi.org/10.1016/j.jma.2022.12.015.
[3] N. Eliaz, Corrosion of metallic biomaterials: A review, Materials 12 (3) (2019) 407, https://doi.org/10.3390/ma12030407.
[4] J. Yang, Z. Zhang, W. Yao, Y. Wu, Y. Gao, Y. Yang, L. Wu, M. Serdechnova, C. Blawert, F. Pan, Recent developments in coatings on biodegradable Mg alloys: A review, J. Magnes. Alloy 13 (4) (2025) 1405–1427, https://doi.org/10.1016/j.jma.2025.01.027.
[5] M.B. Kannan, R.S. Raman, vitro degradation and mechanical integrity of calcium-containing magnesium alloys in modified-simulated body fluid, Biomaterials 29 (15) (2008) 2306–2314, https://doi.org/10.1016/j.biomaterials.2008.02.003.
[6] N. Larrosa, R. Akid, R. Ainsworth, Corrosion-fatigue: a review of damage tolerance models, Int. Mater. Rev. 63 (5) (2018) 283–308, https://doi.org/10.1080/09506608.2017.1375644.
[7] X. Chen, S. Zhou, H. Shi, Y. Wu, T. Chen, W. Huang, Enhancing the mechanical properties and osteogenic differentiation of Mg-1 wt% Ho alloy by tailoring microstructures through extrusion temperatures, J. Mater. Res. Technol. 30 (2024) 6941–6952, https://doi.org/10.1016/j.jmrt.2024.05.094.
[8] M. Hashemi, R. Alizadeh, T.G. Langdon, Recent advances using equal-channel angular pressing to improve the properties of biodegradable Mg-Zn alloys, J. Magnes. Alloy 11 (7) (2023) 2260–2284, https://doi.org/10.1016/j.jma.2023.07.009.
[9] B.P. Zhang, Y.L. Hou, X.D. Wang, Y. Wang, L. Geng, Mechanical properties, degradation performance and cytotoxicity of Mg-Zn-Ca biomedical alloys with different compositions, Mater. Sci. Eng. C. 31 (8) (2011) 1667–1673, https://doi.org/10.1016/j.msec.2011.07.015.
[10] Y. Wan, G. Xiong, H. Luo, F. He, Y. Huang, X. Zhou, Preparation and characterization of a new biomedical magnesium–calcium alloy, Mater. Des. 29 (10) (2008) 2034–2037, https://doi.org/10.1016/j.matdes.2008.04.017.
[11] M. Cihova, E. Martinelli, P. Schmutz, A. Myrissa, R. Schäublin, A.M. Weinberg, P. J. Uggowitzer, J.F. Löffler, The role of zinc in the biocorrosion behavior of resorbable Mg-Zn-Ca alloys, Acta Biomater. 100 (2019) 398–414, https://doi.org/10.1016/j.actbio.2019.09.021.
[12] P. Jiang, C. Blawert, R. Hou, J. Bohlen, N. Konchakova, M.L. Zheludkevich, A comprehensive comparison of the corrosion performance, fatigue behavior and mechanical properties of micro-alloyed MgZnCa and MgZnGe alloys, Mater. Des. 185 (2020), https://doi.org/10.1016/j.matdes.2019.108285.
[13] A. Ma, J. Jiang, N. Saito, I. Shigematsu, Y. Yuan, D. Yang, Y. Nishida, Improving both strength and ductility of a Mg alloy through a large number of ECAP passes, Mater. Sci. Eng. A 513 (2009) 122–127, https://doi.org/10.1016/j.msea.2009.01.040.
[14] Z. Yang, A. Ma, B. Xu, J. Jiang, J. Sun, Corrosion behavior of AZ91 Mg alloy with a heterogeneous structure produced by ECAP, Corros. Sci. 187 (2021) 109517, https://doi.org/10.1016/j.corsci.2021.109517.
[15] E.V. Parfenov, O.B. Kulyasova, V.R. Mukaeva, B. Mingo, R.G. Farrakhov, Y. V. Cherneikina, A. Yerokhin, Y.F. Zheng, R.Z. Valiev, Influence of ultra-fine grain structure on corrosion behaviour of biodegradable Mg-1Ca alloy, Corros. Sci. 163 (2020) 108303, https://doi.org/10.1016/j.corsci.2019.108303.
[16] K. Edalati, A. Yamamoto, Z. Horita, T. Ishihara, High-pressure torsion of pure magnesium: Evolution of mechanical properties, microstructures and hydrogen storage capacity with equivalent strain, Scr. Mater. 64 (9) (2011) 880–883, https://doi.org/10.1016/j.scriptamat.2011.01.023.
[17] X. Zhang, Z. Wang, G. Yuan, Y. Xue, Improvement of mechanical properties and corrosion resistance of biodegradable Mg–Nd–Zn–Zr alloys by double extrusion, Mater. Sci. Eng. B 177 (13) (2012) 1113–1119, https://doi.org/10.1016/j.mseb.2012.05.020.
[18] M. Azeem, A. Tewari, S. Mishra, S. Gollapudi, U. Ramamurty, Development of novel grain morphology during hot extrusion of magnesium AZ21 alloy, Acta Mater. 58 (5) (2010) 1495–1502, https://doi.org/10.1016/j.actamat.2009.10.056.
[19] S. Prithivirajan, S. Narendranath, V. Desai, Analysing the combined effect of crystallographic orientation and grain refinement on mechanical properties and corrosion behaviour of ECAPed ZE41 Mg alloy, J. Magnes. Alloy 8 (4) (2020) 1128–1143, https://doi.org/10.1016/j.jma.2020.08.015.
[20] W. Zhang, L. Tan, D. Ni, J. Chen, Y.C. Zhao, L. Liu, C. Shuai, K. Yang, A. Atrens, M. C. Zhao, Effect of grain refinement and crystallographic texture produced by friction stir processing on the biodegradation behavior of a Mg-Nd-Zn alloy, J. Mater. Sci. Technol. 35 (5) (2019) 777–783, https://doi.org/10.1016/j.jmst.2018.11.025.
[21] V.C. Shunmugasamy, M. AbdelGawad, M.U. Sohail, T. Ibrahim, T. Khan, T.D. Seers, B. Mansoor, vitro and in vivo study on fine-grained Mg–Zn–RE–Zr alloy as a biodegradeable orthopedic implant produced by friction stir processing, Bioact. Mater. 28 (2023) 448–466, https://doi.org/10.1016/j.bioactmat.2023.06.010.
[22] T. Chen, B. Fu, J. Shen, U.F. Suhuddin, B. Wiese, Y. Huang, M. Wang, J.F. dos Santos, J.P. Bergmann, B. Klusemann, Application of novel constrained friction processing method to produce fine grained biomedical Mg-Zn-Ca alloy, J. Magnes. Alloy 12 (2) (2024) 516–529, https://doi.org/10.1016/j.jma.2023.10.007.
[23] C.C. de Castro, J. Shen, J.F. dos Santos, B. Klusemann, Microstructural development of as-cast AM50 during Constrained Friction Processing: Grain refinement and influence of process parameters, J. Mater. Process. Technol. 318 (2023) 118018, https://doi.org/10.1016/j.jmatprotec.2023.118018.
[24] C.C. de Castro, A.M. Neves, B. Klusemann, Effect of thermo-mechanical conditions during constrained friction processing on the particle refinement of AM50 Mg-alloy phases, J. Magnes. Alloy 12 (6) (2024) 2298–2311, https://doi.org/10.1016/j.jma.2024.04.002.
[25] T. Chen, B. Fu, U.F. Suhuddin, T. Shen, G. Li, E. Maawad, J. Shen, J.F. dos Santos, J.P. Bergmann, B. Klusemann, Improving mechanical properties of constrained friction processing Mg-Zn-Ca alloys by modifying texture using multiple pass processing, J. Mater. Sci. Technol. 232 (2025) 209–226, https://doi.org/10.1016/j.jmst.2025.01.026.
[26] A. Hammersley, FIT2D: a multi-purpose data reduction, analysis and visualization program, J. Appl. Crystallogr 49 (2016) 646–652, https://doi.org/10.1107/S1600576716000455.
[27] D. Mei, S.V. Lamaka, C. Feiler, M.L. Zheludkevich, The effect of small-molecule bio-relevant organic components at low concentration on the corrosion of commercially pure Mg and Mg-0.8 Ca alloy: An overall perspective, Corros. Sci. 153 (2019) 258–271, https://doi.org/10.1016/j.corsci.2019.03.039.
[28] Z. Li, D. Cheng, K. Wang, E. Hoglund, J. Howe, B. Zhou, T. Sasaki, T. Ohkubo, K. Hono, Revisited precipitation process in dilute Mg-Ca-Zn alloys, Acta Mater. 257 (2023) 119072, https://doi.org/10.1016/j.actamat.2023.119072.
[29] C. Wang, D. Mei, G. Wiese, L. Wang, M. Deng, S.V. Lamaka, M.L. Zheludkevich, High rate oxygen reduction reaction during corrosion of ultra-high-purity magnesium, npj Mater. Degrad. 4 (1) (2020) 42, https://doi.org/10.1038/s41529-020-00146-1.
[30] G. Song, B. Johannesson, S. Hapugoda, D. StJohn, Galvanic corrosion of magnesium alloy AZ91D in contact with an aluminium alloy, steel and zinc, Corros. Sci. 46 (4) (2004) 955–977, https://doi.org/10.1016/S0010-938X(03)00190-2.
[31] P. Yin, N.F. Li, T. Lei, L. Liu, C. Ouyang, Effects of Ca on microstructure, mechanical and corrosion properties and biocompatibility of Mg–Zn–Ca alloys, J. Mater. Sci. Mater. Med. 24 (2013) 1365–1373, https://doi.org/10.1007/s10856-013-4856-y.
[32] Y. Jeong, W. Kim, Enhancement of mechanical properties and corrosion resistance of Mg–Ca alloys through microstructural refinement by indirect extrusion, Corros. Sci. 82 (2014) 392–403, https://doi.org/10.1016/j.corsci.2014.01.041.
[33] L. Wang, D. Snihirova, M. Deng, B. Vaghefinazari, D. Höche, S.V. Lamaka, M. L. Zheludkevich, Revealing physical interpretation of time constants in electrochemical impedance spectra of Mg via Tribo-EIS measurements, Electrochim. Acta 404 (2022) 139582, https://doi.org/10.1016/j.electacta.2021.139582.
[34] L. Wang, D. Snihirova, M.D. Havigh, M. Deng, S.V. Lamaka, H. Terryn, M. L. Zheludkevich, Non-stationarity in electrochemical impedance measurement of Mg-based materials in aqueous media, Electrochim. Acta 468 (2023) 143140, https://doi.org/10.1016/j.electacta.2023.143140.
[35] Y. Wu, L. Wu, L. Wang, C. Wang, F. Yu, W. Yao, Y. Yuan, Z. Xie, A. Andrej, J. Wang, Electrophoretic deposition of MXene coating on Mg alloy 2, 5 PDCA-LDH film for enhanced anticorrosion/wear, Colloids Surf. A Physicochem. Eng. Asp. 702 (2024) 135043, https://doi.org/10.1016/j.colsurfa.2024.135043.
[36] Y. Wu, H. Wu, L. Wu, Z.-H. Xie, L. Liu, X. Dai, G. Zhang, W. Yao, Y. Li, F. Pan, Influence of electrolyte temperature on morphology and properties of composite anodic film on titanium alloy Ti-10V-2Fe-3Al, Coatings 10 (11) (2020) 1109, https://doi.org/10.3390/coatings10111109.
[37] L. Wang, D. Snihirova, M. Deng, C. Wang, B. Vaghefinazari, G. Wiese, M. Langridge, D. Höche, S.V. Lamaka, M.L. Zheludkevich, Insight into physical interpretation of high frequency time constant in electrochemical impedance

spectra of Mg, Corros. Sci. 187 (2021) 109501, https://doi.org/10.1016/j.corsci.2021.109501.
[38] M. Deng, L. Wang, D. Snihirova, J. Bohlen, G. Kurz, S.V. Lamaka, D. Höche, M. L. Zheludkevich, Micro-alloyed Mg-Ca: Corrosion susceptibility to heating history and a plain problem-solving approach, J. Magnes. Alloy 11 (4) (2023) 1193–1205, https://doi.org/10.1016/j.jma.2022.12.014.
[39] H. Wang, Y. Song, J. Yu, D. Shan, H. Han, Characterization of filiform corrosion of Mg–3Zn Mg alloy, J. Electrochem. Soc. 164 (9) (2017) C574, https://doi.org/10.1149/2.1221709jes.
[40] P. Jiang, C. Blawert, R. Hou, N. Scharnagl, J. Bohlen, M.L. Zheludkevich, Microstructural influence on corrosion behavior of MgZnGe alloy in NaCl solution, J. Alloy. Compd. 783 (2019) 179–192, https://doi.org/10.1016/j.jallcom.2018.12.296.
[41] M. Nienaber, M. Braatz, N.B. Khalifa, J. Bohlen, Property profile development during wire extrusion and wire drawing of magnesium alloys AZ31 and ZX10, Mater. Des. 224 (2022) 111355, https://doi.org/10.1016/j.matdes.2022.111355.
[42] X.N. Ly, S. Yang, Y. Qin, Influence of solid-solution treatment on microstructure, mechanical property and corrosion behavior of biodegradable Mg-Zn-Ca alloy, IOP Conf. Ser. Mater. Sci. Eng. 182 (2017) 012054, https://doi.org/10.1088/1757-899X/182/1/012054.
[43] R.N. Abdullaev, R.A. Khairulin, Y.M. Kozlovskii, S.V. Stankus, A.S. Agazhanov, Density and Thermal Expansion of Magnesium–Calcium Alloys in Solid and Liquid States, Int. J. Thermophys. 44 (5) (2023) 74, https://doi.org/10.1007/s10765-023-03187-1.
[44] A. Maqbool, N.Z. Khan, Microstructure and corrosion behavior of thermo-mechanically processed rare earth Mg alloy: Effect of friction stir processing 359 (15) (2024) 135934, https://doi.org/10.1016/j.matlet.2024.135934.
[45] N. Xu, W.D. Zhang, S.Q. Cai, Y. Zhuo, Q.N. Song, Y.F. Bao, Microstructure and tensile properties of rapid-cooling friction-stir-welded AZ31B Mg alloy along thickness direction, Trans. Nonferr. Met. Soc. China 30 (12) (2020) 3254–3262, https://doi.org/10.1016/S1003-6326(20)65458-9.
[46] M. Cihova, P. Schmutz, R. Schäublin, J.F. Löffler, Biocorrosion zoomed in: evidence for dealloying of nanometric intermetallic particles in magnesium alloys, Adv. Mater. 31 (42) (2019) 1903080, https://doi.org/10.1002/adma.201903080.
[47] P. Jiang, C. Blawert, N. Scharnagl, J. Bohlen, M.L. Zheludkevich, Mechanistic understanding of the corrosion behavior of Mg4Zn0. 2Sn alloys: From the perspective view of microstructure, Corros. Sci. 174 (2020) 108863, https://doi.org/10.1016/j.corsci.2020.108863.
[48] W. Ci, X. Chen, X. Dai, C. Liu, Y. Ma, D. Zhao, F. Pan, Achieving ultra-high corrosion-resistant Mg-Zn-Sc alloys by forming Sc-assisted protective corrosion product film, J. Mater. Sci. Technol. 181 (2024) 138–151, https://doi.org/10.1016/j.jmst.2023.08.068.
[49] W. Ci, Q. Tao, X. Chen, C. Blawert, M. Serdechnova, C. Song, S. Yuan, F. Pan, M. L. Zheludkevich, Enhancing corrosion resistance of Mg-Nd-Zr-In alloys via the development of a triple-layered In (Indium) rich corrosion product film, Corros. Sci. 250 (2025) 112905, https://doi.org/10.1016/j.corsci.2025.112905.
[50] Y. Yu, Y. Shi, C. Zhang, L. Liu, J. Pan, Regulating degradation in MgZnCa metallic glass: Formation of zinc-rich amorphous layer through internal zinc migration, J. Magnes. Alloy 13 (7) (2024) 3346–3356, https://doi.org/10.1016/j.jma.2024.08.015.
[51] Y. Yang, C. Zhang, Y. Peng, Y. Yu, L. Liu, Effects of crystallization on the corrosion resistance of Fe-based amorphous coatings, Corros. Sci. 59 (2012) 10–19, https://doi.org/10.1016/j.corsci.2012.02.003.
[52] Y. Chen, Y. Liu, T. Ying, Y. Yang, J. Wang, X. Xu, Z. Shen, Y. Li, D. Qiu, H. Zhu, J. Wu, G. Zhu, F. Cao, W. Ding, X. Zeng, Stainless magnesium alloy based on self-healing amorphous surface, Mater. Today 92 (2026) 35–43, https://doi.org/10.1016/j.mattod.2025.11.015.
[53] C. Xu, J. Wang, C. Chen, C. Wang, Y. Sun, S. Zhu, S. Guan, Initial micro-galvanic corrosion behavior between Mg_2Ca and α-Mg via quasi-in situ SEM approach and first-principles calculation, J. Magnes. Alloy 11 (3) (2023) 958–965, https://doi.org/10.1016/j.jma.2021.06.017.
[54] L. Moreno, E. Matykina, K.A. Yasakau, C. Blawert, R. Arrabal, M. Mohedano, As-cast and extruded MgZnCa systems for biodegradable implants: characterization and corrosion behavior, J. Magnes. Alloy 11 (3) (2023) 1102–1120, https://doi.org/10.1016/j.jma.2023.02.001.
[55] B. Zhang, X. Ma, A review—Pitting corrosion initiation investigated by TEM, J. Mater. Sci. Technol. 35 (7) (2019) 1455–1465, https://doi.org/10.1016/j.jmst.2019.01.013.
[56] W.M. Haynes, CRC Handbook of Chemistry and Physics, CRC Press, Boca Raton, United States, 2014.
[57] Y.H. Fu, P.W. Chu, Localized corrosion behavior and surface corrosion film microstructure of a commercial dual-phase LZ91 Mg alloy, npj Mater. Degrad. 9 (1) (2025) 19, https://doi.org/10.1038/s41529-025-00567-w.
[58] K.A. Unocic, H.H. Elsentriecy, M.P. Brady, H. Meyer, G. Song, M. Fayek, R. A. Meisner, B. Davis, Transmission electron microscopy study of aqueous film formation and evolution on magnesium alloys, J. Electrochem. Soc. 161 (6) (2014) C302, https://doi.org/10.1149/2.024406jes.
[59] D. Rossouw, D. Fu, D.N. Leonard, M.P. Brady, G.A. Botton, J.R. Kish, Characterization of localized filament corrosion products at the anodic head on a model Mg-Zn-Zr alloy surface, Corrosion 73 (5) (2017) 518–525, https://doi.org/10.5006/2268.
[60] M. Deng, L. Wang, D. Höche, S.V. Lamaka, C. Wang, D. Snihirova, Y. Jin, Y. Zhang, M.L. Zheludkevich, Approaching "stainless magnesium" by Ca micro-alloying, Mater. Horiz. 8 (2) (2021) 589–596, https://doi.org/10.1039/D0MH01380C.
[61] S.K. Woo, B.-C. Suh, H.S. Kim, C.D. Yim, Effect of processing history on corrosion behaviours of high purity Mg, Corros. Sci. 184 (2021) 109357, https://doi.org/10.1016/j.corsci.2021.109357.
[62] D. Song, A. Ma, J. Jiang, P. Lin, D. Yang, J. Fan, Corrosion behavior of equal-channel-angular-pressed pure magnesium in NaCl aqueous solution, Corros. Sci. 52 (2) (2010) 481–490, https://doi.org/10.1016/j.corsci.2009.10.004.
[63] Y. Song, E.-H. Han, D. Shan, C.D. Yim, B.S. You, The role of second phases in the corrosion behavior of Mg–5Zn alloy, Corros. Sci. 60 (2012) 238–245, https://doi.org/10.1016/j.corsci.2012.03.030.
[64] F. Cao, Z. Shi, G.-L. Song, M. Liu, A. Atrens, Corrosion behaviour in salt spray and in 3.5% NaCl solution saturated with Mg $(OH)_2$ of as-cast and solution heat-treated binary Mg–X alloys: X= Mn, Sn, Ca, Zn, Al, Zr, Si, Sr, Corros. Sci. 76 (2013) 60–97, https://doi.org/10.1016/j.corsci.2013.06.030.
[65] L. Tong, Q. Zhang, Z. Jiang, J. Zhang, J. Meng, L. Cheng, H. Zhang, Microstructures, mechanical properties and corrosion resistances of extruded Mg–Zn–Ca–xCe/La alloys, J. Mech. Behav. Biomed. Mater. 62 (2016) 57–70, https://doi.org/10.1016/j.jmbbm.2016.04.038.
[66] H.-Y. Ha, J.-Y. Kang, J. Yang, C.D. Yim, B.S. You, Limitations in the use of the potentiodynamic polarisation curves to investigate the effect of Zn on the corrosion behaviour of as-extruded Mg–Zn binary alloy, Corros. Sci. 75 (2013) 426–433, https://doi.org/10.1016/j.corsci.2013.06.027.
[67] G. Ben-Hamu, D. Eliezer, A. Kaya, Y. Na, K. Shin, Microstructure and corrosion behavior of Mg–Zn–Ag alloys, Mater. Sci. Eng. A 435 (2006) 579–587, https://doi.org/10.1016/j.msea.2006.07.109.
[68] G. Ben-Hamu, D. Eliezer, K. Shin, The role of Mg2Si on the corrosion behavior of wrought Mg–Zn–Mn alloy, Intermetallics 16 (7) (2008) 860–867, https://doi.org/10.1016/j.intermet.2008.03.003.
[69] M. Mandal, A. Moon, G. Deo, C. Mendis, K. Mondal, Corrosion behavior of Mg–2.4 Zn alloy micro-alloyed with Ag and Ca, Corros. Sci. 78 (2014) 172–182, https://doi.org/10.1016/j.corsci.2013.09.012.
[70] Y. Xiong, Y.K. Jiao, X.Q. Zha, Z.G. Chen, T.T. He, S.B. Wang, W. Cao, Effect of Al Addition on Microstructure, Mechanical, and Corrosion Properties of Hot Extruded Mg-2.0 Zn-0.4 Mn Alloy, J. Mater. Eng. Perform. 33 (9) (2024) 4620–4632, https://doi.org/10.1007/s11665-023-08252-2.
[71] C. Gong, X. He, X. Yan, Corrosion behavior of Mg–Ca–Zn alloys with high Zn content, J. Phys. Chem. Solids 152 (2021) 109952, https://doi.org/10.1016/j.jpcs.2021.109952.
[72] A. Bahmani, S. Arthanari, K.S. Shin, Corrosion behavior of Mg–Mn–Ca alloy: influences of Al, Sn and Zn, J. Magnes. Alloy 7 (1) (2019) 38–46, https://doi.org/10.1016/j.jma.2018.11.004.
[73] Y. Hu, Z. Jia, R. Kou, Z. Zhai, X. Niu, Effect of Sn on corrosion properties of homogenized Mg-6Zn-0.25 Ca magnesium alloy, Mater. Teh. 54 (9) (2025) 2345–2351, https://doi.org/10.12442/j.issn.1002-185X.20240160.
[74] P. Jiang, C. Blawert, M.L. Zheludkevich, The corrosion performance and mechanical properties of Mg-Zn based alloys—a review, Corros. Mater. Degrad. 1 (1) (2020) 92–158, https://doi.org/10.3390/cmd1010007.